Earth, Planets and Space

FULL PAPER

Open Access

Long-duration seismicity and their relation to Copahue volcano unrest

Ivan Melchor[1*], Javier Almendros[2], Marcia Hantusch[1], Sergey Samsonov[3], Dominique Derauw[1,4,5], Enzo Martínez[1] and Alberto Caselli[1]

Abstract

Understanding seismic tremor wavefields can shed light on the complex functioning of a volcanic system and, thus, improve volcano monitoring systems. Usually, several seismic stations are required to detect, characterize, and locate volcanic tremors, which can be difficult in remote areas or low-income countries. In these cases, alternative techniques have to be used. Here, we apply a data-reduction approach based on the analysis of three-component seismic data from two co-located stations operating in different times to detect and analyze long-duration tremors. We characterize the spectral content and the polarization of 355 long-duration tremors recorded by a seismic sensor located 9.5 km SE from the active vent of Copahue volcano in the period 2012–2016 and 2018–2019. We classified them as narrow- (NB) and broad-band (BB) tremors according to their spectral content. Several parameters describe the characteristic peaks composing each NB episode: polarization degree, rectilinearity, horizontal azimuth, vertical incidence. Moreover, we propose two coefficients C_P and C_L for describing to what extent the wavefield is polarized. For BB episodes, we extend these attributes and express them as a function of frequency. We compare the occurrence of NB and BB episodes with the volcanic activity (including the level of the crater lake, deformation, temperature, and explosive activity) to get insights into their mechanisms. This comparison suggests that the wavefield of NB tremors becomes more linearly polarized during eruptive episodes, but does not provide any specific relationship between the tremor frequency and volcanic activity. On the other hand, BB tremors show a seasonal behavior that would be related to the activity of the shallow hydrothermal system.

Keywords: Tremor characterization, Data reduction methods, Non-eruptive tremor, Copahue volcano

*Correspondence: ifmelchor@unrn.edu.ar
[1] Instituto de Investigación en Paleobiología y Geología, Universidad Nacional de Río Negro–CONICET, General Roca, Argentina
Full list of author information is available at the end of the article

Graphical Abstract

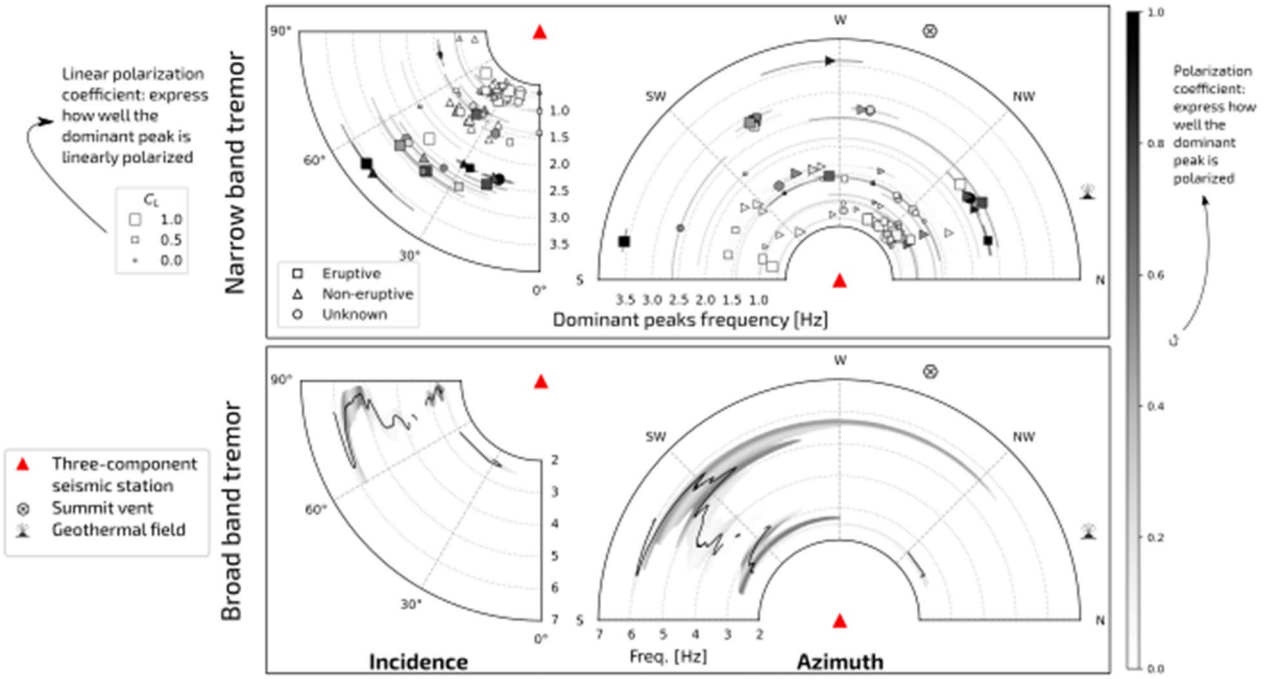

Introduction

Volcanic tremors are sustained long-period seismic signals related to the internal flow dynamics of fluids feeding volcanic and hydrothermal systems (Ferrick et al. 1982; Julian 1994). Due to its relation to eruptive activity, its detection and location are central for assessing hazard mitigation, especially during volcanic unrest (McNutt and Nishimura 2008; Chouet and Matoza 2013; Tárraga et al. 2014). Generally, volcanic tremors have a spectral-peaked nature, showing one peak (monochromatic) or multiple peaks, which can be harmonics of a fundamental period (harmonic tremor) or not (non-harmonic tremor) (Konstantinou and Schlindwein 2003). Moreover, volcanic tremors usually change in amplitude and spectral content over time, which is mainly attributed to source effects (Hotovec et al. 2013; Ogiso et al. 2015; Jolly et al. 2020). Tracking the characteristics of the tremor wavefield has allowed the development of conceptual models of the geometry and dynamics of the volcanic feeding system (Almendros et al. 2014; Unglert and Jellinek 2015) and eruptive conduits (Ogiso et al. 2015; Yukutake et al. 2017; Konstantinou et al. 2019).

Apart from being a continuous signal, volcanic tremors can be composed of short-duration events in a temporally dense swarm (Almendros et al. 1997) or emerging as regular, cyclic increases of amplitude (Cannata et al. 2010). This latter case is referred to as "banded" tremor and is usually associated with a hydrothermal origin (Fujita 2008). One of the well-accepted hypotheses about the origin of volcanic tremors is they are flow-induced oscillations (Rust et al. 2008). A wide variety of mechanisms have been proposed to explain volcanic tremors: transient hydraulic pressure pulses (Seidl et al. 1981); resonant scattering by fluid-filled cavities (McMechan 1982), acoustic resonance in fluid-filled conduits (Chouet 1986), hydrothermal boiling (Leet 1988); non-linear flow effects in magmatic conduits (Julian 1994); gas coalescence in the crater vent (Ripepe and Gordeev 1999); pressure perturbations in a bubble-rich magma (Neuberg and O'Gorman 2002); hydrothermal two-phase flow instabilities (Fujita 2008); or periodic pressure perturbations triggered by permeable gas flow (Girona et al. 2019), among others (Montegrossi et al. 2019; Gestrich et al. 2020; Takeo 2021).

The detection and location of volcanic tremors are mostly based on seismic networks, either applying cross-correlation between station pairs (Droznin et al. 2015; Li and Gudmundsson 2020) or by using a small-aperture seismic array (Ferrazzini et al. 1991; Almendros et al. 2004). Once the tremor is detected, several methods, such as the amplitude distribution, can be used for location (Ichihara and Matsumoto 2017), whereas analyzing the associated wavefield provides insights into their source mechanism. However, applying these methods

requires several stations deployed around the volcano, which may be difficult in remote areas (Jiménez Morales et al. 2017; Naismith et al. 2019; Park et al. 2021) and expensive in low-income countries (Ayele et al. 2007; Goitom et al. 2015; Barrière et al. 2019).

When only a single three-component (triaxial) seismic station records the volcanic tremor, several analyses exist for its characterization, such as measuring the nonlinearity (Konstantinou and Schlindwein 2003) or scaling behavior (Benoit et al. 2003; Konstantinou et al. 2019) of the component with the lower signal-to-noise ratio. While detecting short-duration episodes (of the order of seconds to minutes) is usually achieved by a visual inspection of the seismogram, longer durations may require applying data reduction methods (DRM) (Carniel 2014; Melchor et al. 2020; Caudron et al. 2021). This approach extracts successive features in short-length windows that can be parametric (such as the root mean square of the amplitude) or vectorial (such as the power spectrum density). Thus, DRM allows the detection and characterization of long-duration tremors. In these situations, the location of the tremor is not possible unless more information is known, such as with eruptive tremors (McNutt and Nishimura 2008). Therefore, polarization analysis is the only method that allows inferring the direction of propagation of the waves composing the tremor through reducing the information of the three components of the seismogram into several attributes that describe the 3-D particle displacement (Anderson and Nehorai 1996).

In this work, we focused on dissecting and characterizing the spectral content and polarization properties of long-duration (>1 h) tremor episodes, and comparing their characteristics with the activity of Copahue. Seismic data were acquired by two triaxial stations co-located at 9.5 km from the active vent. The approach followed here represents a forward step for long-duration tremor characterization using a triaxial sensor, and it can be applied to enhance our ability to investigate the volcanic system using limited seismic networks.

Copahue volcano and seismic data

Copahue volcano is an active polygenetic stratovolcano of basaltic–andesitic composition located in the intra-arc region of Southern Andes Volcanic Zone (37°51′S, 71°11′W, Fig. 1) (Folguera et al. 2016). The crater hosts a highly active hyperacid lake with complex dynamics that depend on the interactions between volcanic gases and meteoric waters from rain, snow, and the glacier that melts and discharges into the crater (Agusto et al. 2017). In recent years, the activity of Copahue volcano has been characterized by strombolian activity with sporadic

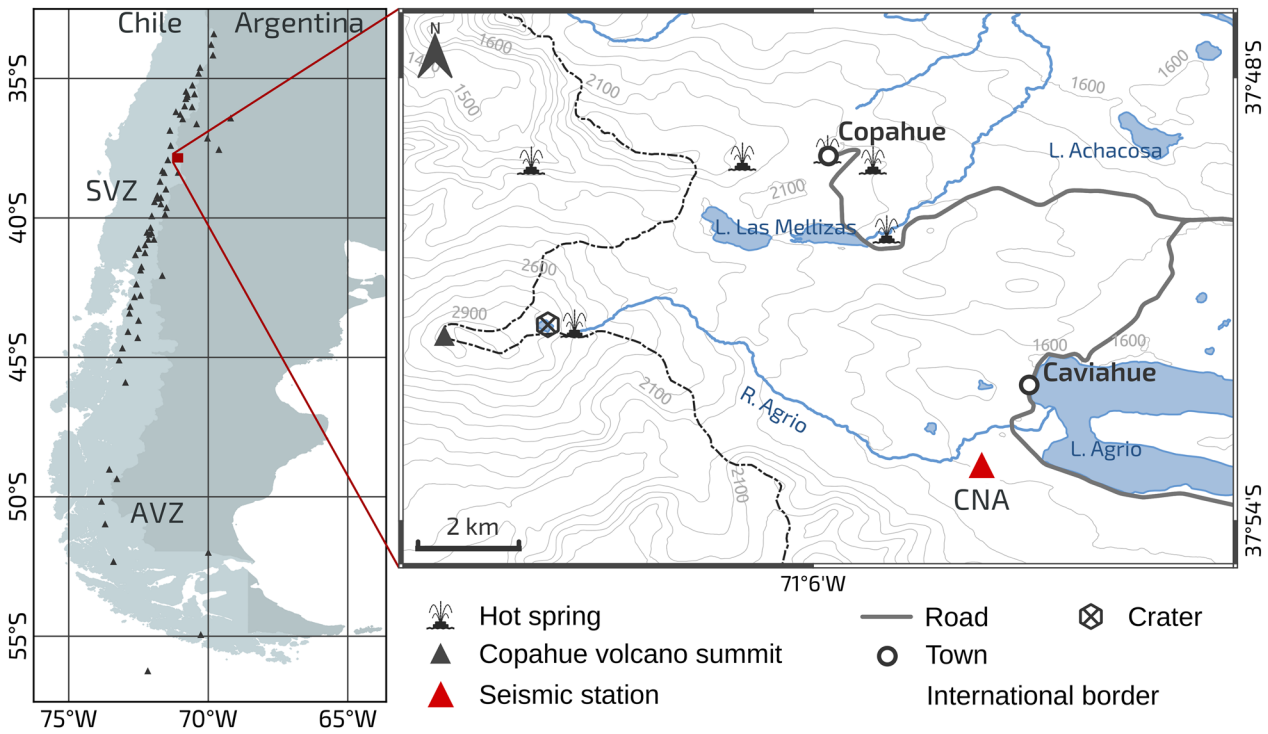

Fig. 1 Geotectonic setting for Copahue Volcano. At left, the geotectonic setting of Southern Volcanic Zone (SVZ) and Austral Volcanic Zone (AVZ). At right, the map locates the active crater, the seismic station (CNA), and the main geothermal areas

low-energetic phreatic and phreatomagmatic eruptive pulses (Caselli et al. 2016; Hantusch et al. 2021a), continuous changes in the volume, temperature, and chemical composition of the crater lake (Agusto et al. 2017; Candela-Becerra et al. 2020), high degassing rates (Tamburello et al. 2015), and a continuous inflationary processes (Velez et al. 2016; Lundgren et al. 2017).

The Copahue volcano is hosted by an old (4–5 Ma) 15 × 20 km, active volcano-tectonic depression, known as Agrio Caldera. A fault-controlled geothermal system located 4 km to the NW of Caviahue town (Fig. 1) (Lamberti et al. 2019; Barcelona et al. 2019) has shown to be seismically active, producing both volcano-tectonic events (Montenegro et al. 2021) and volcanic tremors (Ibañez et al. 2008; Melchor et al. 2020).

Seismic data were collected by two co-located seismic stations composed of triaxial sensors 9.5 km SE from the crater: a short period (1 s) and a broad-band (20 s). Both sensors, which are called CNA in Fig. 1, operated at different times and controlled by a 24-bit A/D converter sampling at 100 Hz. The short-period sensor is part of the seismic network of the National Institute of Seismic Prevention (INPRES) of Argentina, and available data correspond to the period between 1 June 2012 to 31 December 2016 with some gaps. On the other hand, the broad-band sensor is part of the National University of Rio Negro (UNRN) seismic network, and continuous data have been recorded since 1 January 2018.

Detection of tremor episodes

Data preprocessing for the detection of long-duration tremors consisted of applying data reduction methods (DRM) to the three components of the seismogram in the range of 0.5–10 Hz. The idea behind this approach is to track relevant information associated with the long-term volcanic process perturbing the local ambient wavefield (Tárraga et al. 2014). We followed the procedure described in Melchor et al. (2020) for computing energy, permutation entropy, spectrogram, and *polargram* in successive 20-min windows.

The permutation entropy is an information-theory measure introduced by Bandt and Pompe (2002) that measures the complexity of a time series. This parameter has proved to be a suitable parameter for distinguishing tremor and noise bursts at Copahue volcano (Melchor et al. 2020). Unlike spectrogram, which stacks successive power spectral density (PSD) functions over time, polargram stacks polarization-degree (PD) functions. Using these two vectorial DRMs simultaneously allows visually detecting long-duration tremors in long time windows of weeks to months (Melchor et al. 2020).

Thus, the detection of long-duration tremors was achieved visually by inspecting the time evolution of reduced parameters. For this study, we established a specific definition for tremor episode, requiring a period longer than 1 h with (1) energy above its background; (2) permutation entropy beneath its background level (being this the mode of the corresponding year), and (3) spectral content showing well-defined ranges that correlate with high polarization degree. Thus, when these conditions were given, the period was classified as a tremor episode (Melchor et al. 2020).

In total, we found 355 episodes that satisfied these conditions. We classified them as narrow- (NB) or broad-band (BB) according to the shape of their spectral content. The former group has a spectral content characterized by single or multiple peaks, whereas the second shows a broad frequency range.

Characterization of tremor episodes

For the characterization of tremors, we followed a similar approach to their detection. First, we divided the three-component seismogram of each tremor episode into 1-min windows. Then, we re-sampled at 40 Hz, removed the trend and instrumental response, and tapered using a 20% Tukey window. We computed the power spectral density (PSD) of the vertical component using the *multitaper* algorithm (Prieto et al. 2009), which is based on multiplying data by different weights (so-called tapers). Finally, we derived the frequency-dependent polarization attributes using the three components of the seismogram, which are: polarization degree PD, rectilinearity R, horizontal azimuth Θ_H, and vertical incidence Θ_V (see Appendix 1).

Narrow-band tremor

We identified approximately 7986 h of NB tremor, distributed in 85 episodes. In general, NBs are low-amplitude with an unclear onset and end. As the duration of NB episodes varies from 1 to 10^3 h, we applied a moving average to reduce the time dimension (i.e., the number of 1-min windows) of the frequency-functions DRM shaping each episode. The chosen window length was proportional to their duration, as shown in Table 1.

Table 1 Moving-average window applied for different duration ranges

Duration [h]	Moving-average window [min]
< 20	1
20–40	2
40–105	4
105–300	8
> 300	40

From each PSD, we extracted all frequency peaks with energy above 95% of the maximum, from now on called *samples*. Then, we estimated the normalized probability density function (PDF) of all samples weighted by their spectral energy. The frequencies characterizing the NB episodes are all those peaks with a normalized density above 0.6.

Additionally, for each sample, we computed the average and standard deviation σ of PD, R, Θ_H, and Θ_V in the frequency range $\pm$ 0.05 Hz centered at the central frequency of the sample. Where PD$\geqslant$0.8, and σ_{PD} and σ_R are $\leqslant$0.1 (i.e., when the sample is well-polarized), we estimated the normalized PDFs of R from all averages lying $\pm$ 0.1 Hz around the characteristic frequencies. Likewise, PDFs of Θ_H and Θ_V were estimated when $R \geqslant 0.7$, and σ_H and σ_V were $\leqslant 5°$ (i.e., for linearly polarizations). Thus, for each polarization parameter (i.e., R, Θ_H, and Θ_V) describing each characteristic frequency of the NB episode, we extracted their range, defined as the difference between the minimum and maximum value of the normalized PDF at 0.5, and mode.

Figure 2 shows an example of a 16-h NB tremor that occurred in July 2019, whereas Fig. 3 depicts the followed characterization. Figure 2a and b shows the time evolution of the energy and spectral energy of samples. Note that the energy in 2a correlates with the spectral peak around 1.4 Hz in 2b. In fact, this is the only peak above 0.6 in the corresponding PDF (Fig. 3a) and, thus, the only characterizing frequency of the episode.

Figure 2c and d shows the time evolution of PD and R averages when samples are well-polarized (i.e., PD$\geqslant$ 0.8, $\sigma_{PD} \leqslant 0.1$, and $\sigma_R \leqslant 0.1$). Only those samples in the range $\pm$0.1 Hz around the 1.4-Hz peak define the PDF that characterizes the peak rectilinearity. The well-polarized 1.4-Hz peak shows a bimodal distribution (Fig. 3b) with values from circular ($\leqslant$ 0.3) to linear ($\geqslant$ 0.7), being elliptical (0.3 to 0.7) the most probable polarization. Similarly, Fig. 2e and f shows the time evolution of Θ_H and Θ_V when $R \geqslant$0.7, and $\sigma_H, \sigma_V \leqslant 5$ is satisfied, whereas Fig. 3c and d shows the PDFs corresponding to the 1.4-Hz peak. The difference between the minimum and maximum values in the Θ_H PDF shows a large dispersion, in contrast to the Θ_V that centers at $\sim 78°$.

Note that in Fig. 2, the number of samples of each attribute (from now on sample size) changes. Indeed, this value also characterizes the peaks of tremor episodes. We defined N_T as the sample size of the spectral PDF and N_P the sample size lying in the range $\pm$ 0.1 Hz around each characteristic peak. Similarly, we also define N_R, N_H, and N_V as the sample size characterizing the R, Θ_H, and Θ_V of the peak, as shown in Fig. 3. Although the 1.4-Hz peak is well-polarized with 792 N_R of the 998 N_P characterizing it, only 98 N_H and 86 N_V describe the polarization ellipse, i.e., around 1% of N_R.

Therefore, we can define the polarization coefficient of a characteristic peak as

$$C_P = \frac{N_R}{N_P} \tag{1}$$

to express to what extent the characteristic peak is well polarized over the episode. Likewise, we define

$$C_L = \frac{N_H + N_V}{2\,N_R} \tag{2}$$

as the coefficient that expresses to what extent the characteristic peak is linearly polarized.

Thus if a specific peak of an NB tremor has $C_P \sim 1$ and $C_L \sim 1$, it is well and linearly polarized, and the parameters Θ_H and Θ_V can be tracked over the episode. Otherwise, if C_P is low and C_L high, linearly polarized transient waves compose the tremor. In the tremor of Fig. 2, the 1.4-Hz peak is characterized by a C_P of 0.8 and C_L of 0.1, which means the peak is well-polarized but not linearly, as noted in Fig. 2d.

Results

In total, we found 205 peaks in the range 0.6–3.6 Hz for the 85 NB episodes, of which 12 (~14%) showed a monochromatic spectrum and 61 (~72%) displayed two or three peaks. In fact, only 179 (~87%) peaks were well-polarized with a C_P associated, i.e., $N_R \neq 0$, of which 94 (~46%) had a $C_P > 0.25$. Moreover, only 25 peaks showed a C_P value greater than 0.75. The frequencies of the peaks with higher C_P were found above 1.0 Hz.

From the 179 peaks with a C_P associated, 75 (~35%) had a $C_L \neq 0$, of which 58 had a $C_L > 0.25$, and 20 a $C_L > 0.75$. We found a slight trend of increasing the frequency as C_L and C_P jointly increase (Fig. 4a). Below 2 Hz, peaks with high C_L and low C_P were observed.

The polarization attributes of 19 polarized peaks with $C_P > 0.5$ and with $C_L \neq 0$ are shown in Fig. 4b. At horizontal incidence ($\Theta_V > 70$), only two peaks were found with low C_L, whereas below 20°, linearly polarized peaks, i.e., large C_L, were found with a narrow azimuthal range. Only 11 have frequencies in the range 2.4–2.9 Hz, whereas eight lie in the range 0.9–1.6 Hz. Our results showed scattered azimuthal angles. Nevertheless, five peaks at 2.4 Hz and one at 2.5 Hz showed similar azimuths and incidence in the range 14–33° and 15–27°, respectively. Additional file 1 provides all this information for the 85 NB episodes.

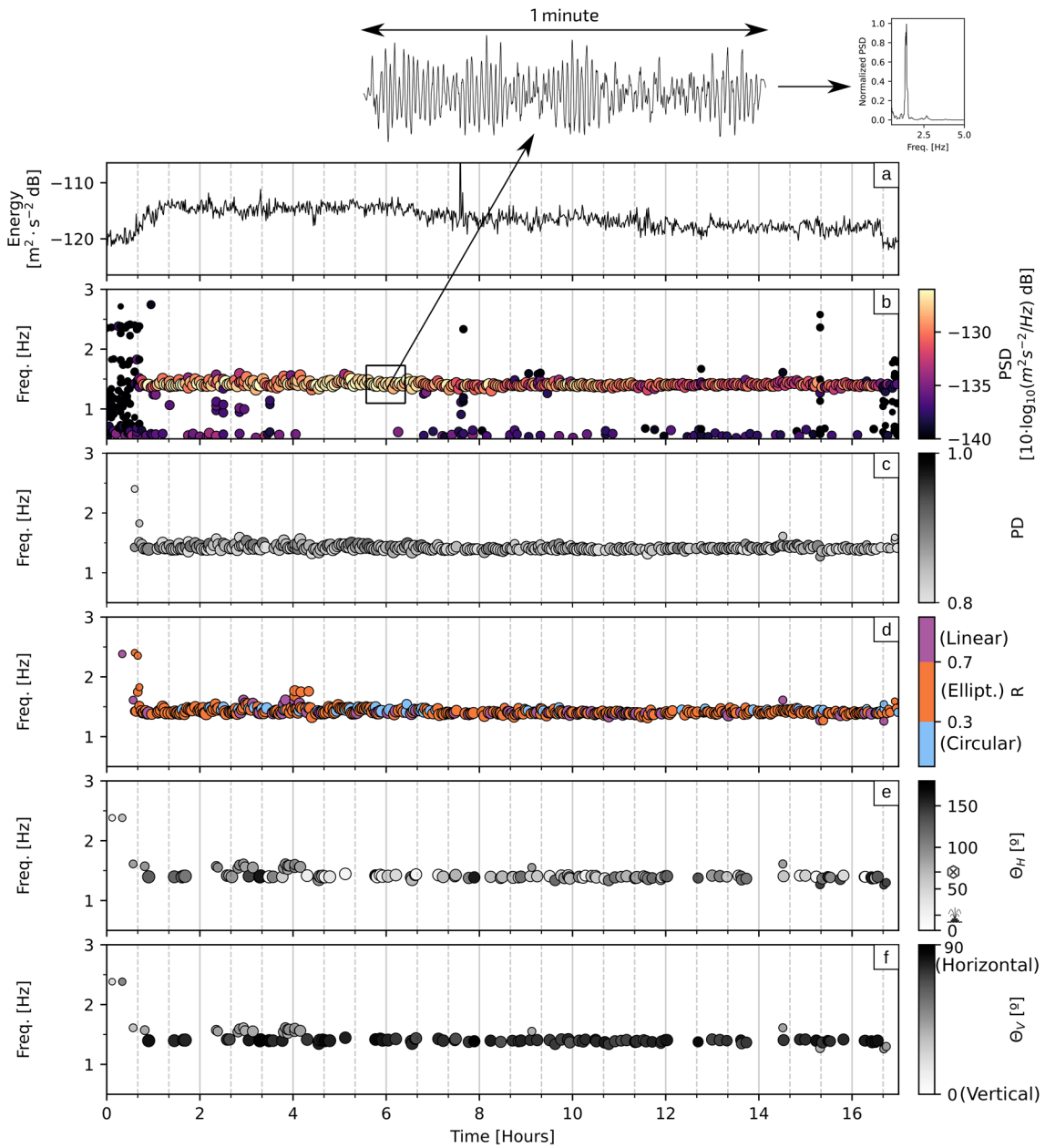

Fig. 2 Time evolution of reduced parameters for the NB episode occurred at 23:40:00 UTC on 21 July 2019. **a** Energy in the range 0.5–10 Hz. **b** Spectral peaks with energy above 95% of the maximum, i.e., samples. **c** Averaged polarization degree (PD) of each sample in the range ±0.05 Hz when PD$\geqslant$ 0.8 and $\sigma_{PD} \leqslant 0.1$. **d** Averaged rectilinearity (R) of each sample in the range ±0.05 Hz when $\sigma_R \leqslant 0.1$. **e** Averaged horizontal azimuth (Θ_H) and **f** vertical incidence (Θ_V) of each sample when $R \geqslant 0.7$ and $\sigma_H, \sigma_V \leqslant 5°$. Due to the large number of samples, only the third part of the information is depicted in **b** and **c**. The size of each circle is proportional to its spectral energy, given in **b**

Second-order features

The approach followed in the characterization of NB episodes did not consider all the observed characteristics. The parametrization of "second-order" features requires a different approach that we do not treat here. However, we shall mention three main behaviors observed in the time evolution of some NB episodes: secondary high-rectilinearity peaks, low-intensity frequency shift, and "seismic silences".

Secondary peaks are short-duration and/or low-energetic enough for exceeding 0.6 in the normalized PDF. For example, Fig. 5 shows a tremor episode characterized

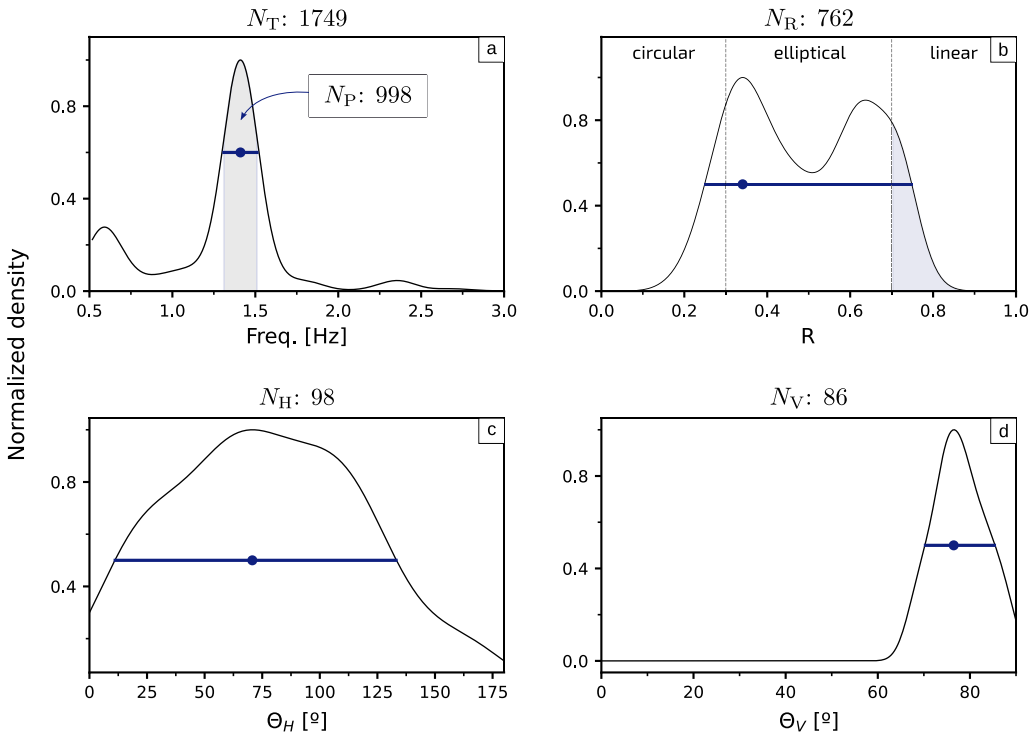

Fig. 3 Statistical analysis for the NB episode of Fig. 2. **a** The normalized PDF of the samples and weighted by their spectral energy. The peak centered at 1.4 Hz, which is the only peak above 0.6, is the characteristic peak of the episode. The normalized PDF of averaged rectilinearities R (**b**), horizontal azimuth Θ_H (**c**), and vertical incidence Θ_V (**d**) in the range $\pm$0.1Hz around the characteristic peak. R, Θ_H, and Θ_V characterize the polarization of the peak by extracting the mode and range of each distribution. The range is the width of the distribution at 0.5 (blue horizontal lines in **b**–**d**). The upper part of each plot gives the sample size of each PDF

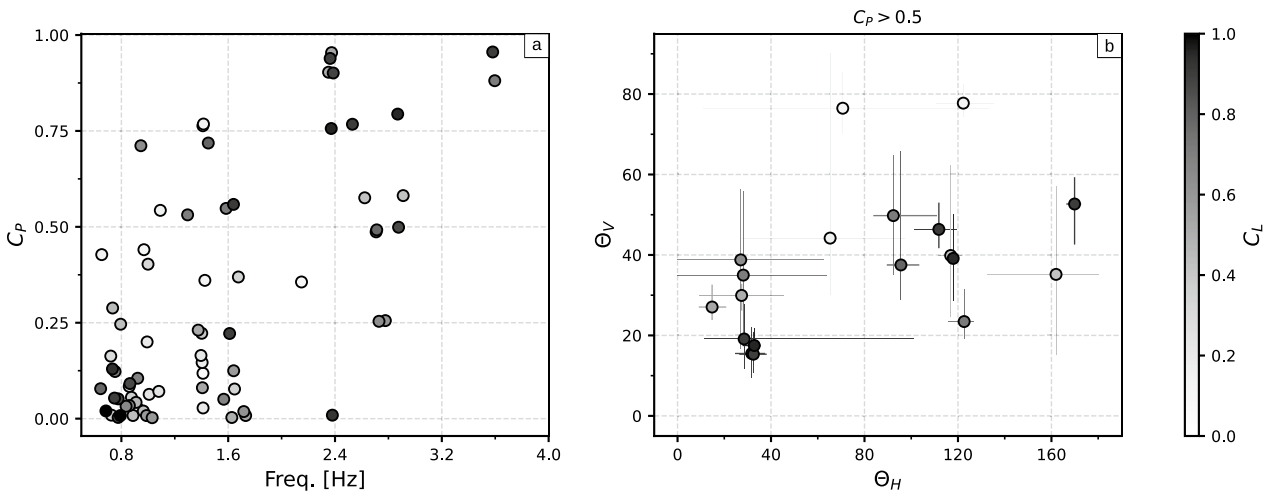

Fig. 4 **a** C_P in function of the frequency of peaks and C_L. **b** Azimuth and Incidence for peaks with $C_P > 0.5$

by two circularly polarized spectral peaks at 1.0 and 1.4 Hz. The energy of the NB episode gradually increases and reaches maximum values past 15 h (Fig. 5a), dominated by the 1-Hz peak (Fig. 5b). When this peak began to decrease in frequency, a linear peak around 1.6 Hz appeared (Fig. 5b and 5c). However, its duration and energy were too weak to cross the 0.6-threshold in the

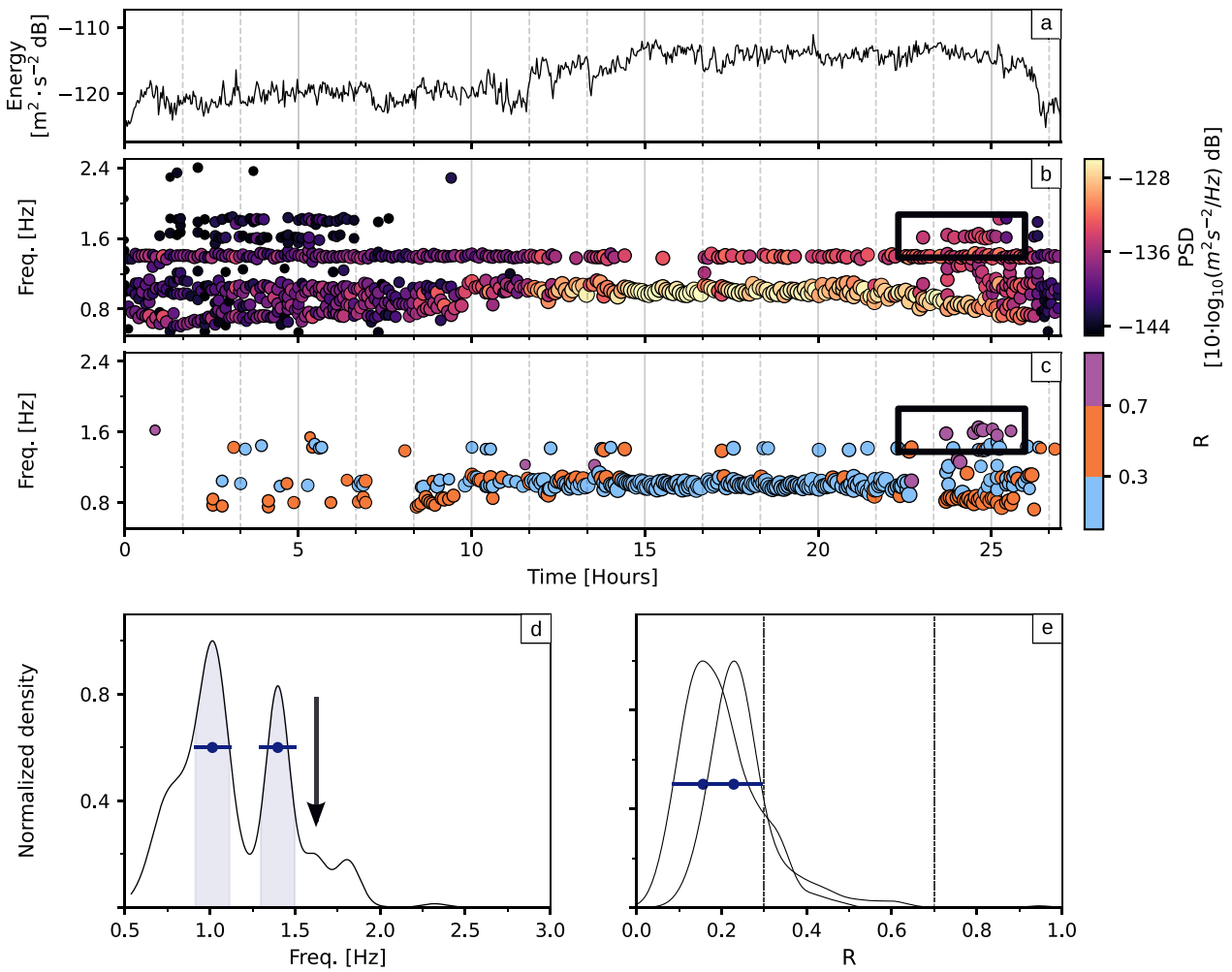

Fig. 5 The NB tremor occurred at 01:20:00 UTC on 01 January 2015. **a** Energy in the range 0.5–10 Hz. **b** Spectral peaks with energy above 95% of the maximum. **c** Averaged rectilinearity (R) of each sample in the range ±0.05 Hz when σR⩽0.1. The normalized PDF of averaged horizontal azimuth $\Theta H\Theta_H$(**d**), and vertical incidence $\Theta V\Theta_H$ (**e**) in the range ±0.1 ±0.1Hz around the characteristic peaks. Black rectangular boxes in **b** and **c** show the 1.6-Hz secondary peak that is filtered in the statistical analysis in **d**

PDF (Fig. 5d), and no polarization attributes were analyzed (Fig. 5e).

The 1-Hz peak in Figure 5 also shows a low frequency shift, which is known as "gliding effect" (Hotovec et al. 2013). We observed this effect in 14 peaks characterizing 14 NB episodes (Additional file 1), all of them below 1.5 Hz. Only one gliding peak was linearly polarized with a C_L of 0.4. The rest had values of C_P in the range 0.2–0.8. In all cases, the shifts do not exceed 1.0 Hz, such as in the above example on which the 1-Hz peak glides down 0.2 Hz in five hours; consequently, we termed them as "low-intensity gliding". Moreover, in NB episodes characterized by two or more frequencies, the gliding effect only affected one frequency, such as in the example.

The term "seismic silences" was first introduced by (Morales et al. 2015) to describe the behavior of the tremor before the ash emissions of Copahue in October 2014. These episodes showed periods with a sudden decrease of amplitude, like a "silence", of around 40 min. We have observed a similar pattern in 14 (~16%) episodes since February 2013 (Fig. 6). Although we do not have evidence that all NBs with "seismic silences" occurred before ash emissions in the analyzed period (Additional file 1), the eruptive tremor of July 2020 showed a similar variation in amplitude (Hantusch et al. 2021b).

Broad-band tremor

Long periods of energetic and high PD values in a continuous range of frequencies characterize BB tremors, which are the most characteristic seismic signal observed with a total of 270 episodes in the analyzed period. Most of them emerged in swarms of tens of episodes lasting from

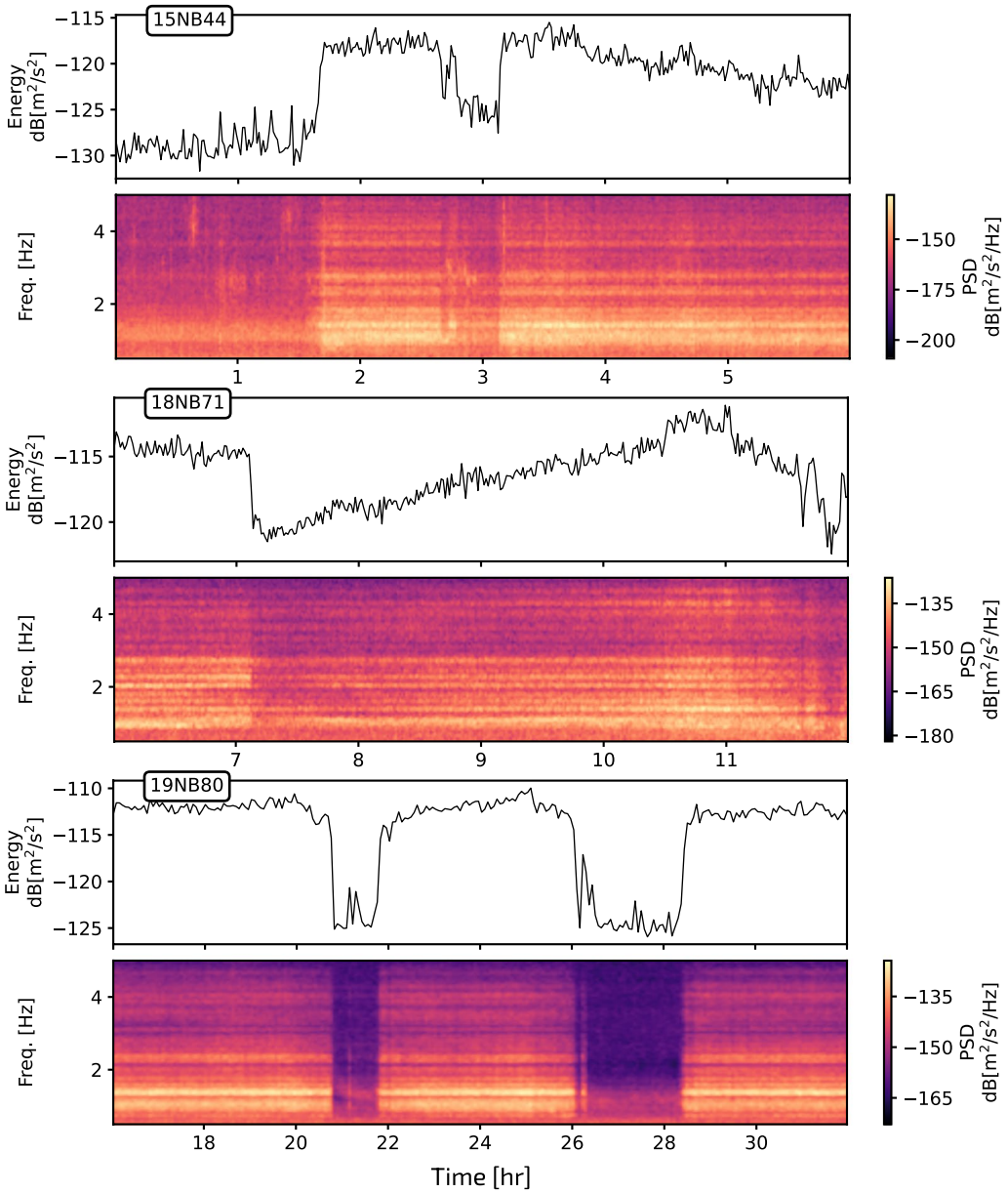

Fig. 6 Examples of "seismic silences" during long-duration NB tremors. The attributes of these tremors can de documented in Additional file 1 by searching for the codes shown at the top left of each plot

days to months. The longest (99 days) was composed of 40 episodes (Table 2). Counting them was simple since they showed regular periods of occurrence centered at 12 h with onset times in the range 13:00–19:00 UTC (Fig. 7).

Swarm episodes showed a regular seasonality by generally occurring in spring. This high periodicity and seasonality led us to consider that BB tremors are caused by a seasonal cycle and modulated by diurnal variations. Therefore, we compared BB episodes with meteorological data provided by the Interjurisdictional Watershed Authority (http://www.aic.gob.ar) of Argentina. However, we did not find any hint of correlation with temperature, wind speed or direction, snowfall, or rain (Additional file 7).

The similarities in the spectral content (Fig. 7c) suggest a common source. Thus, we followed a different approach to characterize their polarization attributes. First, we characterized each episode by computing the energy e, dominant frequency f_d, and frequency range f_{range} in the most probable PSD (pPSD) of the vertical

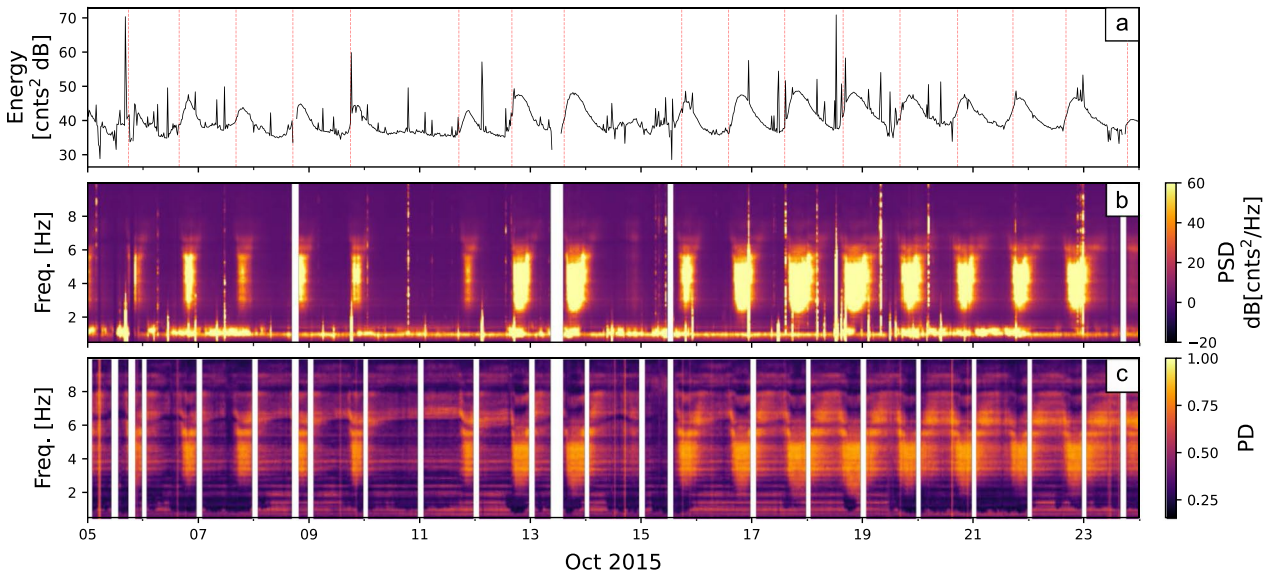

Fig. 7 Several days of October 2015 on which a BB swarm occurred. **a** Energy of vertical component in the range 0.5–10 Hz. **b** Successive 20-min (**b**) PSD and **c** PD side by side. Vertical red horizontal bars represent the onset of the BBs. A periodicity of 26.7 ± 8.3 h characterized it

component. The procedure consisted of stacking all 1-minute PSDs and extracting the spectral mode in the PDF by frequency (see Additional file 2 for details). Figure 8 shows an example of the followed procedure. Figure 8a shows the temporal evolution of the energy in successive 1-min windows, whereas in Fig. 8b we can see the 1608 PSDs composing the tremor and the pPSD. Note that the pPSD does not show a smooth variation since it expresses the mode of the spectral PDFs over frequency.

The pPSD in Fig. 8b suddenly rises around 2.5 Hz, 0.5-Hz after reaching a relative minimum. We considered this minimum as the spectral onset of the tremor; consequently, we define the frequency range f_{range} by tracing a horizontal line from this minimum until it intersects the pPSD again. The dominant frequency f_d is, then, defined as the mode of the distribution in the f_{range}, and the energy e is the area between the pPSD and −160 dB (Fig. 8c).

The energy of BB tremors spanned from 5 to 90 dB without showing a clear central value. Individual episodes have, in general, higher values of energy. Most of the episodes lasted less than 20 hr. However, the longest was recorded during the 2013 swarm, lasting several days. Concerning its dominant frequency, most of them are found in the range 4–6 Hz, with no relationship with energy or duration. Additional file 1 also summarizes the characteristics of the 270 BB episodes.

Table 2 Periods of time on which BB tremor emerge in swarms and volcanic activity observed in the crater (Additional files 3, 4)

Start date	Duration [days]	Nro. episodes	Surficial activity
2012 Dec 18	9	8	Strombolian eruption of VEI 2
2013 Aug 27	14	8	–
2013 Oct 13	40	20	Ash emissions, explosions, no lake
2014 Sep 27	45	28	Ash emissions, explosions, no lake
2015 Sep 28	75	57	Ash emissions, explosions, no lake
2016 Sep 03	4	3	Ash emissions, no lake
2018 Aug 25	96	40	Ash emissions, no lake
2019 Sep 11	75	53	Ash emissions, explosions

Polarization analysis

Polarization attributes were, then, statistically analyzed for all BB episodes available by stacking all frequency-dependent polarization attributes in their respective f_{range}. Figure 9 shows the results. Figure 9a depicts 25th, 50th, and 75th percentiles of stacked rectilinearity as a function of the frequency when PD $\geqslant$ 0.8. The 50th percentile varies between 0.3 and 0.7 and shows sporadic peaks above 0.7, which indicates that the polarization of BB tremors is almost elliptical. At frequencies above 6 Hz, the polarization turns circular, reaching a minimum of 0.2 at ~6.4 Hz.

Similar to NB tremors, we define the sample size as a function of the frequency according to R values. Thus,

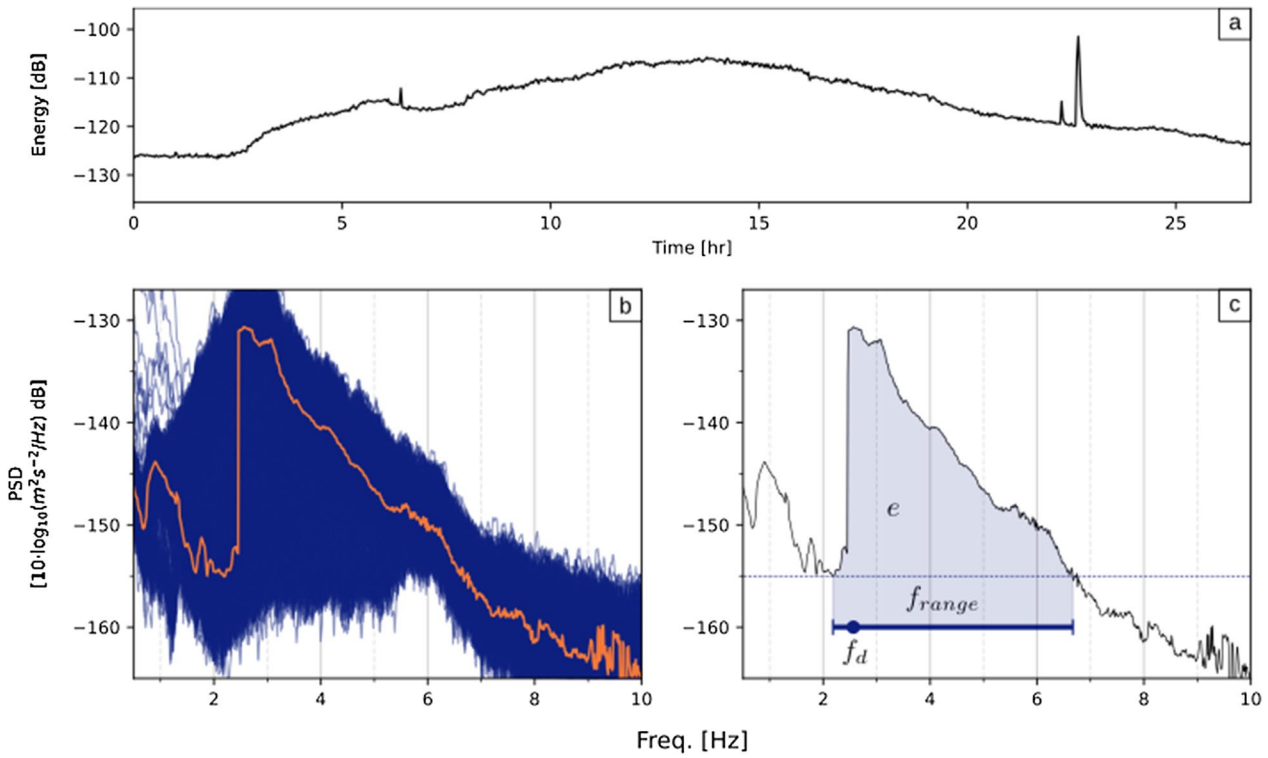

Fig. 8 The broad-band tremor occurred at 09:20:00 UTC on 1 June 2012. **a** Time evolution of the energy in the range 0.5–10 Hz. **b** The 1608 1-min PSD composing the episode along with the most probable PSD (pPSD), in orange. **c** Schematic representation of the measures of dominant frequency f_d, frequency range f_{range}, and energy e

we denoted the sample size of linear ($R \geqslant 0.7$), elliptical ($0.3 < R < 0.7$), and circular ($R \leqslant 0.3$) rectilinearity as N_L, N_E, and N_C. Note that the total sample size of R, i.e., $N_L + N_E + N_C$, depends on the frequency since the f_{range} of each BB episode varies (Fig. 9b). We found the higher number of N_E in the range 3.5–5.1 Hz and at peaks centered at 5.5 and 6.1 Hz. On the other hand, the higher values of N_L lie in the range 4.5–6.0 Hz and at peaks centered at 3.0 and 4.1 Hz.

C_P and C_L are also estimated for BB tremors (Fig. 9c). The maximum value of C_P is ~0.5 at 4.7 Hz and corresponds to a C_L of 0.18. The peaks with highest values of C_L have lower values of C_P, which means that the few well-polarized samples are linear. To exclude individual episodes in the characterization of Θ_H and Θ_V, we applied a cut-off of $1.2 \cdot 10^4$ in the sample size since it is the maximum number of 1-min intervals that a BB episode could have (Fig. 9d and e). Our results show that the 50th percentile of Θ_H orientates in the direction SW–NE for frequencies below 5.5 Hz. Above 5 Hz, the range between 25th and 75th percentiles becomes wider, whereas the 50th percentile moves tens of degrees south at 6 Hz. On the other hand, Θ_V defines a sub-horizontal polarization in the range of 60–90°.

Discussion

To get insights into the source mechanism behind NB and BB tremors, information about the volcanic activity is essential. For example, eruptive tremors occur during eruptive periods, and they have particular characteristics (McNutt and Nishimura 2008). Before comparing the occurrence of observed tremors with the volcanic activity, we shall evaluate whether non-volcanic sources can also generate similar seismicity.

Many studies have shown that rivers (Díaz et al. 2014) and glaciers (Roeoesli et al. 2016) are prone to generate long-duration seismicity with tremor-like spectral content. However, due to the lack of large rivers and glaciers around the seismic station, these sources are not suitable candidates to explain the NB and BB tremors at Copahue. Other possible source is induced ambient noise during strong winds. However, associated wavefield are characterized by high-entropy, unpolarized particle motions, and homogeneous spectrum (Melchor et al. 2020). Therefore, we interpret that both NB and BB episodes must be driven by volcanic or hydrothermal processes.

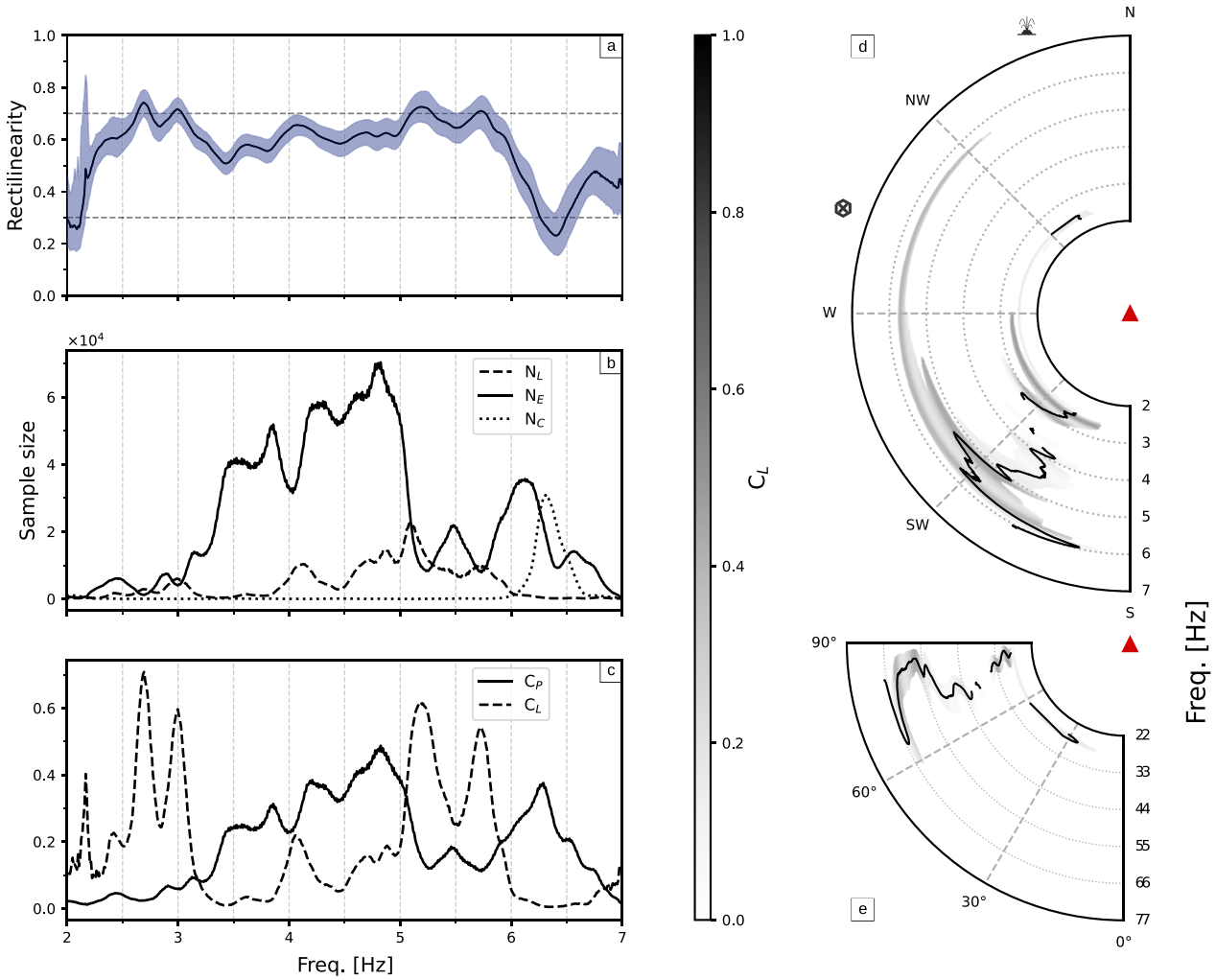

Fig. 9 Polarization analysis of 226 BB tremor episodes. We excluded 44 episodes due to gaps or/and corrupted data in some of the three components. **a** The 25th, 50th (black line), and 75th percentiles of R when PD$\geqslant$ 0.8. **b** The sample size of R in function of the frequency and polarization class: linear (N_L), elliptical (N_E), and circular (N_C). **c** The polarization coefficients C_P and C_L in function of the frequency. **d** The 25th, 50th (black line), and 75th percentiles of horizontal azimuth Θ_H and (e) vertical incidence Θ_V in function of C_L when the sample size is greater than 10^3

Copahue activity

We chronologically constructed the volcanic activity timeline from different sources and available data to compare it with tremor occurrence. The detailed activity of Copahue in the 2012–2019 period was obtained from reports of the Chilean Southern Andean Volcano Observatory (OVDAS) and the Global Volcanism Program (GVP), which periodically summarize seismic and infrasonic events, deformation, and surficial activity (Additional file 3). We also tracked the deformation of the Copahue volcano using the descending synthetic aperture radar (SAR) imagery acquired during 2011–2019 by the RADARSAT-2 satellite. The time series of cumulative displacements in the line-of-sight (LOS) direction was computed for each acquisition epoch, and the linear rate was estimated using linear regression.

The SO_2 emission of Copahue is continuously tracked by the Global Sulfur Dioxide Monitoring Group (https://so2.gsfc.nasa.gov), which publishes almost daily OMI and TROPOMI-based images of SO_2 vertical column density at middle tropospheric altitudes (5–7.5 km). We reviewed all available images to classify periods of "High", "Low", or "No" SO_2 emissions.

Thermal and infrared bands of LANDSAT 7 and 8 with high spatial resolution led us to estimate the Land Surface Temperature (LST) in the crater. Indeed, we tracked the maximum LST (from now on symbolized as MVT) value inside the crater over time. Finally,

ash emission and the presence/absence of the crater lake were estimated by observation of LANDSAT 7, 8, and Sentinel S2 true-color images. Additional files 3 and 4 contain specific details of the methods and data, respectively.

Figures 10, 11, 12 compare the time evolution of eruptive activity with NB and BB episodes. The rows in Fig. 10, 11, 12a depict, from top to down, whether the crater lake was present or not, the intensity of the SO_2 anomaly, the presence of ash around the crater, and the explosions reported. Figures 10, 11, 12b and 10, 11, 12c show the deformation in the LOS-direction of the satellite and the MVT, respectively.

The LOS-displacement time series represents the evolution of the inflationary process centered NW from the crater, coinciding with the geothermal field. A two-source system has been proposed to explain this behavior (Velez et al. 2016; Lundgren et al. 2017). Both studies coincide in the presence of a shallow, elongated ~2.5km conduit beneath the active crater connected with a magmatic reservoir at 7–9 km depth below the surface. Moreover, (Lundgren et al. 2017) proposes that (*i*) the shallow conduit is above the hydrothermal system and (*ii*) the magmatic reservoir has an elongated pipe-like shape plunging 25° to the east, reaching the center of the caldera. We observe that the inflationary process that stopped in 2016 activated in the last quarter of 2019 (Fig. 12b).

Except for the ash emissions in 2016, when high values of MVT were observed, possibly, due to the high temperatures of the gas plume, the highest values of MVT coincides with the presence of the crater lake. Moreover, we observed a correlation between these two series from mid-first to second quarters of 2014, 2018, and 2019. In these periods, the progressive decrease of MVT coincides with the crater lake's subsequent disappearance. Similarly, the gradual increase of MVT coincides with the lake's subsequent formation in the following periods: December 2013 to January 2014, June 2018 to January 2019, and in the last months of 2014 and 2019. The temperature and volume of the crater lake depends on the balance between inputs (volcanic fluids and gases and meteoric water from a glacier that is constantly supplying) and outputs (evaporation, seepage, and other processes (Hurst et al. 2015)). We noted a seasonality with the crater lake forming in summer, possibly, due to an increase in the volume of water caused by the thaw.

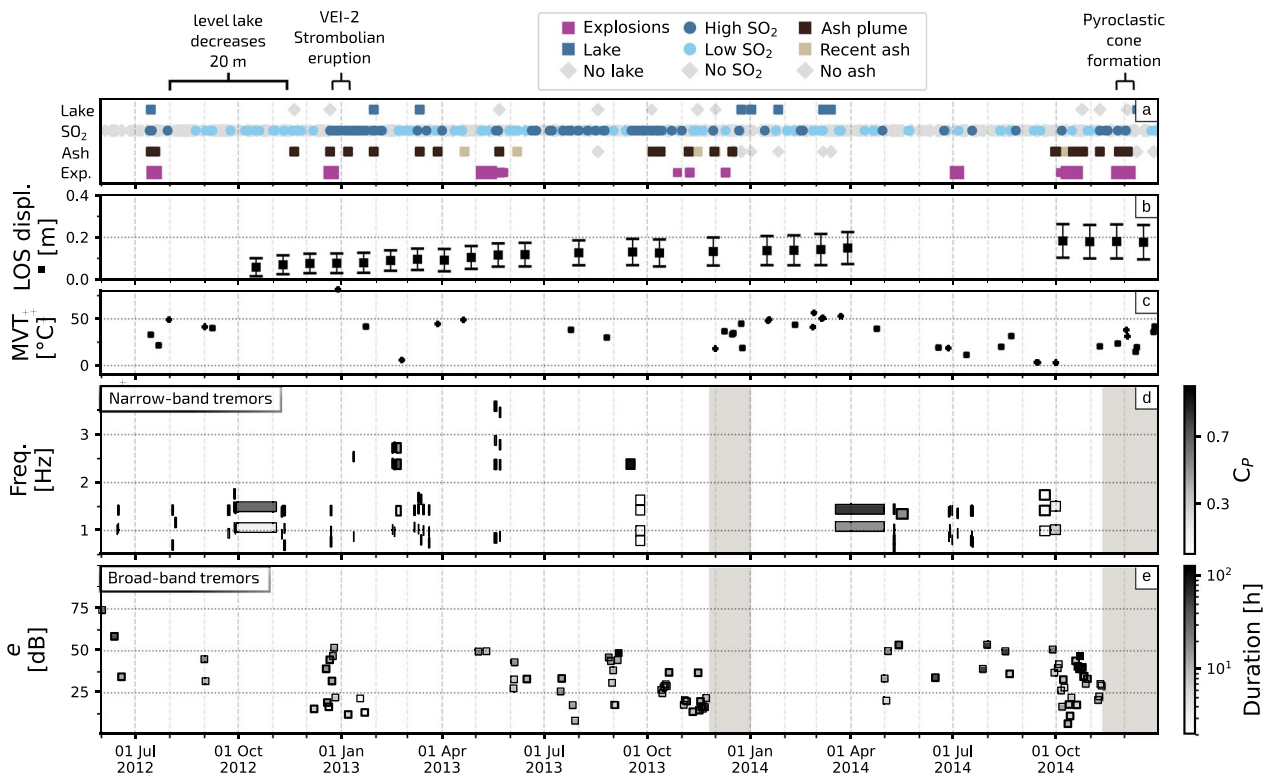

Fig. 10 Time evolution of (**a**) surficial activity, **b** LOS-displacement, **c** LST temperature, **d** frequency and C_P of dominant frequencies of NB tremors, and **e** energy of BB tremors for the periods June 2012 to December 2014. Gray shadows in c and d depict periods without seismic data

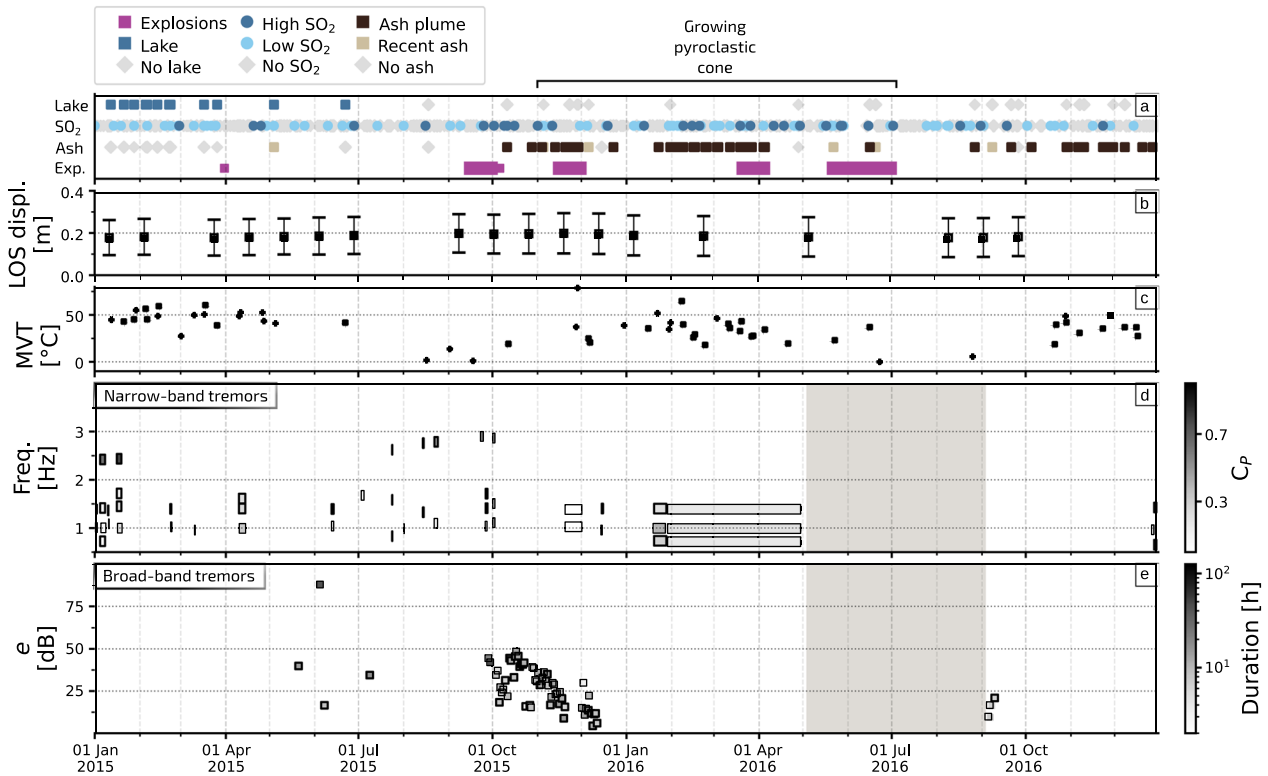

Fig. 11 Time evolution of (**a**) surficial activity, **b** LOS-displacement, **c** LST temperature, **d** frequency and C_P of dominant frequencies of NB tremors, and **e** energy of BB tremors for the periods January 2015 to December 2016. Gray shadows in c and d depict periods without seismic data

Eruptive and non-eruptive tremors

The chronological description of the Copahue's activity led us to classify BB and NB episodes as eruptive or non-eruptive, providing insights into their origin. We classified them as eruptive (E) when they coincide with a period classified as "Ash Plume", "Recent ash", "High SO_2", or "Explosions" (see Figs. 10, 11, 12d). Conversely, when they coincide with a period of "Low SO_2", "No SO_2", or "No Ash", tremor episodes are classified as non-eruptive (NE). In case of no information during the occurrence of the tremor, this is classified as unknown (UK). The classification was done manually by comparing the accumulated duration of each tremor episode and the number of days of activity (see Additional file 5: Table S4). In total, we classified 18 E, 42 NE, and 25 UK episodes.

NB tremors

Before discussing the difference of E, NE, and UK episodes, it is worth pointing out the observed independence in the frequency peaks of the NB episodes. For example, the 1.4 and 1.0-Hz peaks, which are the most common, can appear alone (as monochromatic episodes) or within other peaks. Moreover, observed gliding only affected one peak in episodes with multiple frequencies. This suggests that the frequencies characterizing the non-monochromatic episodes should be considered independently and not as harmonics of a fundamental period. With this in mind, we can classify as eruptive or non-eruptive either NB episodes and characteristic frequencies (see Additional file 5: Table S5).

Most of the peaks showed low values of PD and, therefore, low C_P. This can occur by an increase in isotropic noise or interference with other sources. When, for example, wind speed is high, both isotropic noise and surface waves increase in the wavefield, leading to the appearance of polarized directions modes in the complex space (Greenhalgh et al. 2018). This mechanism would affect all the frequencies alike since wind increases noise at a wide spectral band (Withers et al. 1996). However, the ambient noise could be polarized at specific frequencies by site effects, interfering with the tremor wavefield and reducing the C_P of some peaks. This can explain the low values of C_P below 1 Hz, both for E and NE peaks (Additional file 5: Tables S6, S7). On the other hand, the loss of R produces low C_L values. We observed that the range of R, defined as the distance between their minimum and maximum value (see Figs. 3d and 5e), is low at frequencies above 2 Hz. This suggest that both E and NE

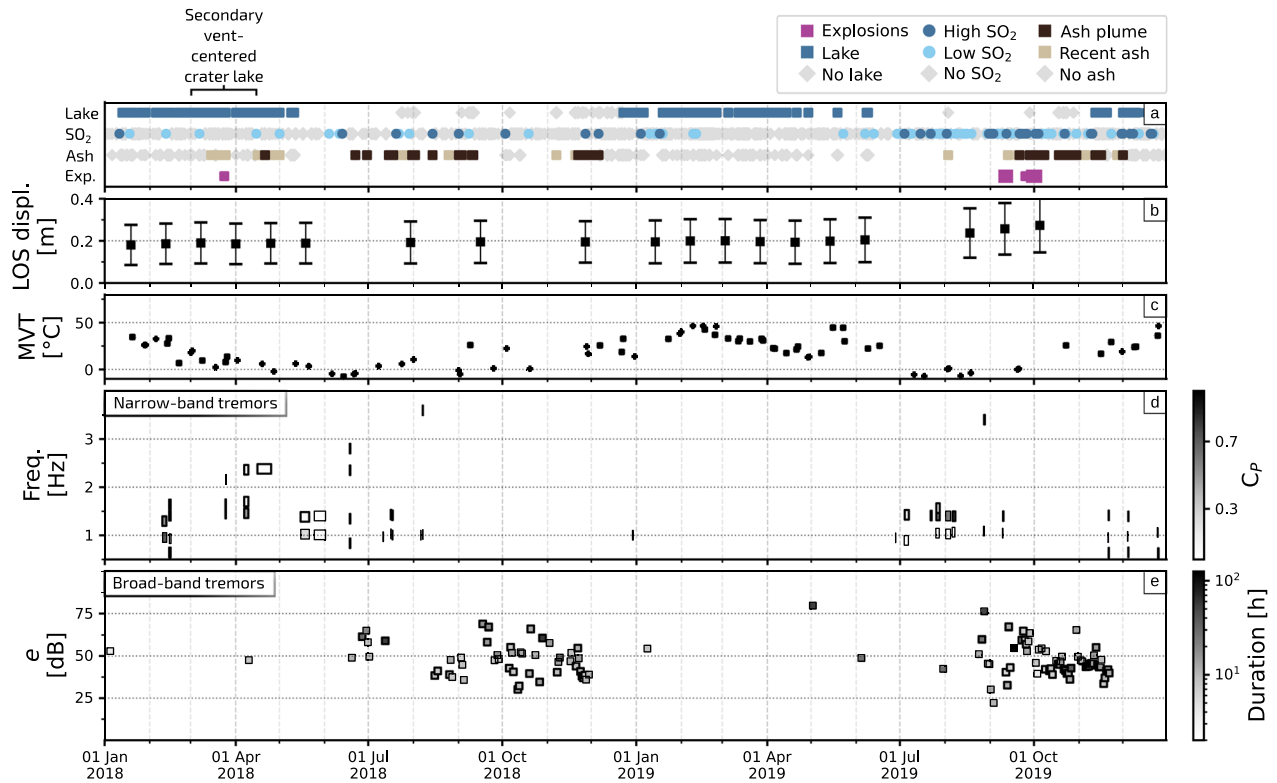

Fig. 12 Time evolution of **a** surficial activity, **b** LOS-displacement, **c** LST temperature, **d** frequency and C_P of dominant frequencies of NB tremors, and **e** energy of BB tremors for the periods January 2018 to December 2019. Gray shadows in c and d depict periods without seismic data

peaks are more affected by scattering effects, noise, multipathing, or seismic interference (Neuberg and Pointer 2000; Hellweg 2003; Greenhalgh et al. 2008; Almendros et al. 2012) below that frequency. Large values of the range of R may also suggest that the tremor wavefield is composed of multiple polarizations, as have been observed in other volcanoes (Goldstein and Chouet 1994; Saccorotti et al. 2004; Almendros et al. 2014).

A comparison between the number of E and NE peaks with $C_P \neq 0$ and $C_L \neq 0$ (Additional file 6: Figs. S6–S8) shows that E peaks are more linearly polarized (~56%) than NE (~37%), suggesting an increase of body waves in the wavefield during eruptive activity. E peaks have no particular characteristics that distinguish them from NE peaks and, therefore, a relationship between surface activity with the frequency of NB episodes cannot be stated (Fig. 13). In general, both E and NE peaks have the same number of occurrences. Thus, there is not clear evidence that a particular frequency, e.g., 1.5 Hz, is linked with ash emissions or intense degassing (see Additional fie 5: S5). For example, peaks at 0.7, 1.0, and 1.5 Hz characterize both the 22 December 2012 strombolian eruption (Fig. 10) and the continuous ash emissions in February–June 2016 (Fig. 11). However, these frequencies are also excited during quiescent periods. Moreover, Θ_H and Θ_V values for the frequencies of those E episodes are similar but also for NE episodes (see Additional file 1).

In general, Θ_H and Θ_V of E, NE, and UK peaks do not show clear patterns when they are compared (see Additional file 5: Tables S6–S8 and Additional file 6: Figs. S1–S4). We interpret these result as strong path or site effects controlling the wavefields. If we also define the range of Θ_H and Θ_V as the absolute difference between their minimum and maximum value in the PDF (see Fig. 3e and f), we noted these values decrease as C_P, C_L, and frequency increases (Fig. 13 and Additional file 6: Fig. S2, S4), being the peaks with frequencies above 2 Hz those with shortest azimuth ranges. This suggests that the peaks below the 2 Hz are more influenced by path effects.

The time evolution of the Θ_H reveals remarkable patterns (Figs. 13c and Additional file 6: Fig. S6). In 2012 and 2013, frequency peaks showed an azimuth direction of ~50°, whereas 2013 and 2018, albeit also present azimuths around this angle, spread its direction in a wider range (see Additional file 6: Fig. S6). This last observation can, therefore, reflect changes in the source or path conditions.

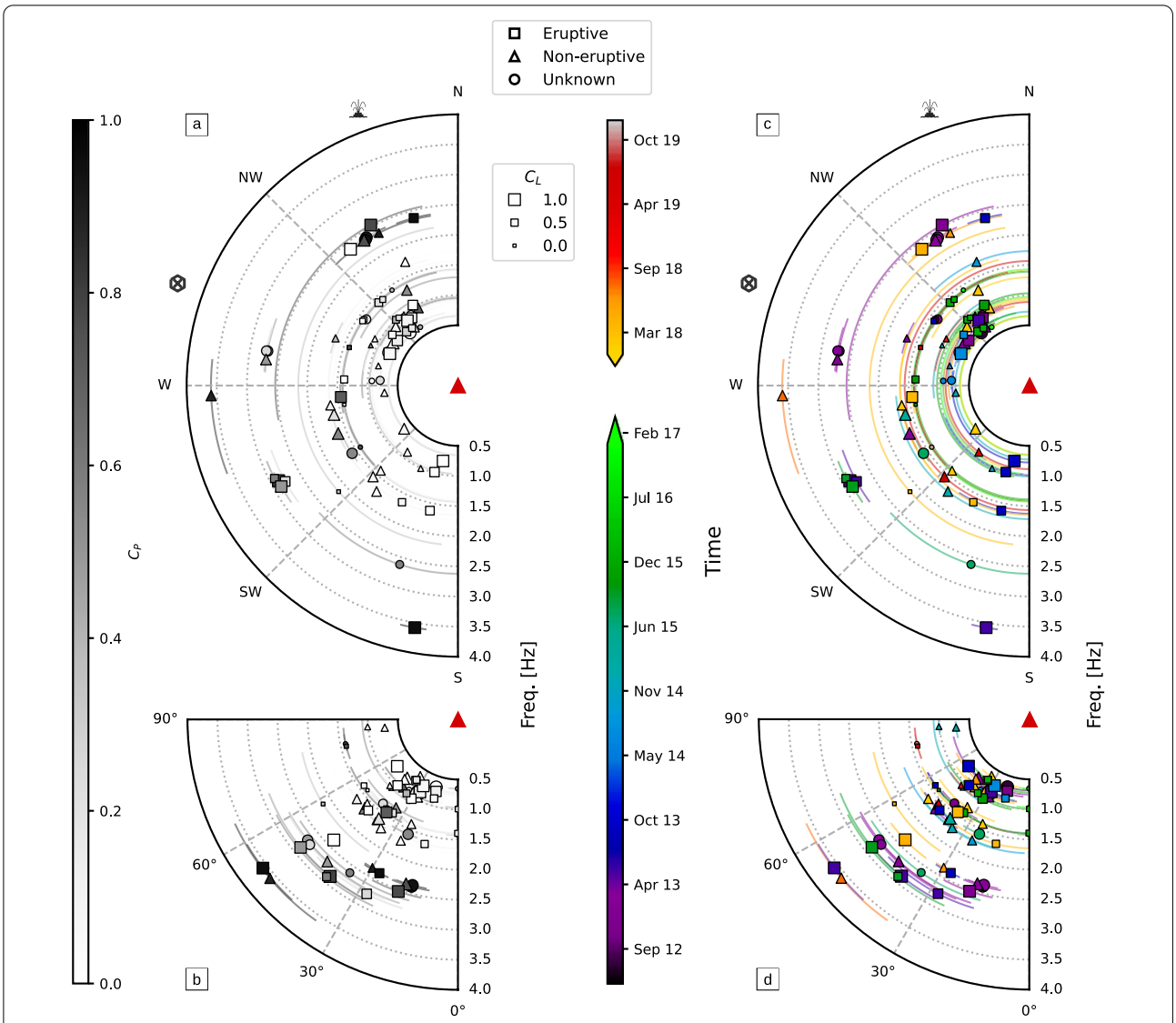

Fig. 13 Polarization attributes in frequency for all dominant peaks of NB tremors. (up) Horizontal azimuth (down) vertical incidence according to definition in Fig. 3

BB tremors

The similarity of BB episodes suggests a common source. However, they not always coincide with eruptive activity. For this reason, we do not consider this tremor as eruptive. Nevertheless, it is worth making some observations about their relationship with ash emissions. BB tremors show seasonal behavior, with 70% of the episodes occurring in spring (see Additional file 5: Table S9). This season is also characterized by the highest number of days with ash emission and without crater lake (Additional file 6: Figs. S1 and S2).

We observed BB episodes 4 days before the 22 December 2012 eruption; 3 days before the explosive activity of 5 March 2013; 8 days before the explosions of 28 October 2013 (Fig. 10); 6 days before the explosions of 5 October 2014; during the explosions of September 2015 (Fig. 11); 3 days before the ash emissions of 22 June 2018; and during the explosions of September 2019 (Fig. 12). In these periods, they emerged in swarms with a trend to decrease their energy. Conversely, BB tremors also occurred without any sign of unrest at posterior periods. Thus, we cannot consider these tremors as a precursor of explosive activity but related to the internal dynamics of the volcano.

Implications for the source of NB tremor

The peaked spectra of NB tremors are commonly viewed as a result of a flow-induced oscillations triggered by instabilities in the magmatic or hydrothermal systems. The seismic radiation released in the interface with elastic medium propagates to the seismic receiver, leading to the duration of the tremor depending on the energy losses by elastic radiation and dissipation processes at the source (Chouet and Matoza 2013).

Eruptive episodes suggest a long-lived mechanism related to activity in the open conduit. For example, a possible explanation for the 2196-hr-long tremor related to 2016 ash emissions is the pressure turbulence in the vent (McNutt and Nishimura 2008). In non-eruptive episodes, long-duration tremors can be explained by acoustic resonance in closed pipe-like conduits filled with low-viscosity fluids (Neuberg et al. 2000). However, the presence of an extended hydrothermal system (Barcelona et al. 2019) can also suggest a different origin, such two-phase flow instabilities or hydrothermal boiling. Another mechanism able to explain the long-duration of NB episodes is the superposition of successive short-duration events too close together in time to be distinguished or a recursive feedback mechanism of long-period seismicity (Neuberg et al. 2006). However, this mechanism produces harmonics through the Dirac comb effect that are unseen in the records.

The observed seismic silences cannot be only attributed to changes in the pressure conditions during ash emissions (Morales et al. 2015) since it also was observed in NE episodes. To gain insight into the mechanism behind these silences, more seismic stations are required.

Polarization attributes provide insights into the propagation direction of the tremor wavefield. However, the use of a three-component sensor to identify that direction is insufficient unless assuming that the major semi-axis of the polarization ellipse is parallel to the direction of propagation (Anderson and Nehorai 1996). Indeed, only when the tremor wavefield is composed of P-waves and the medium is laterally homogeneous, Θ_H and Θ_V point out the source direction.

The most striking result is that NB episodes reveal neither a characteristic spectral pattern nor a clear relationship between their frequencies and surficial activity. This may suggest different but interconnected source origins, or a complex heterogeneous medium. At frequencies around 2.4 Hz, Θ_H centers 20° north (Fig. 13a and c), pointing towards the geothermal field, which has proved to be a source of long-duration seismicity (Ibañez et al. 2008). However, we also observed frequencies from eruptive and non-eruptive NB episodes with similar azimuths, which suggest strong path effects. Another possibility is that those eruptive frequencies are composed of S-waves and, thus, the propagation direction is 110°, coinciding with the crater-receiver direction. On the other hand, the high Θ_V (Fig. 13b and d) means that the propagation direction of the linear polarized waves composing the NB episodes has a vertical incidence, which reinforces the idea of strong heterogeneities along the propagation paths.

The hydrothermal nature of BB tremor

The origin of BB tremor seems to be different from NB tremor. As stated above, the correlation between BB episodes and ash emissions (see Table 2) is close enough to suggest their origin involves internal volcanic processes. By analogy with banded tremors observed in other volcanoes (Cannata et al. 2010; Fujita 2008), we speculate BB tremor is triggered by instabilities of the hydrothermal system beneath the crater of Copahue, which behaves like a steam-water mixture system (Varekamp et al. 2009).

The observed seasonality is therefore easily explained by the recharge–discharge cycles of the hydrothermal system. This seasonality can affect the rate of the long-period seismicity (Nakano and Kumagai 2005; Park et al. 2019) and generate banded tremors (Gresta et al. 1996; Cannata et al. 2010). For example, in Mt. Etna, banded tremors occur mainly in springtime and this behavior was attributed to the recharge of the aquifer by snow melting at the summit of the volcano (Gresta et al. 1996). In this scenario, many factors can explain the duration and energy of BB episodes, including system geometry, the amount of water, and heating rate involved (Fujita 2008). For example, the reduction of the hydrothermal system or the input heat flux would explain the low presence of BB episodes in 2016 or the observed decreasing energy of BB episodes in the swarms (Figs. 10d and 11d).

The polarization attributes are consistent with this conceptual model (Fig. 9). The rectilinearity R shows a mixture of polarized waves in the wavefield (Fig. 9b), possibly due to a high contribution of surface waves. The low values of Θ_V suggest a sub-horizontal incidence, which is interpreted as a shallow source, whereas Θ_H points out in the SW direction (Fig. 9c), i.e., around 90° from the direction of the crater. Thus, we interpret this as S-waves propagating transversely from the crater. The increase of the azimuth range with frequency can be explained by scattering effects (Hellweg 2003).

The broader spectral content of BB tremor suggests a complex source mechanism, which is poorly understood. A simple attempt to explain it would be by the composition with other sources, such as assuming that the brittle failure of the rocks constraining the fluid by pressure changes causes the higher frequencies of the spectrum. On the other hand, changes in the seismic velocity of the system can also cause spectral peaks to shift, leading to

a broader spectral content in the seismic record (Neuberg and O'Gorman 2002). This last mechanism has been used to explain the broad spectrum of the volcanic tremors recorded at Bromo (Gottschämmer 1999) or White Island (Sherburn et al. 1998), among others.

Conclusion

Copahue is a highly active volcano in Southern Andes with low-energy strombolian-like activity dominated by sporadic emission of ash plumes and high degassing rates. We analyzed the continuous seismic data from June 2012 to December 2016 and January 2018 to December 2019 and distinguished 85 narrow-band (NB) and 270 broad-band (BB) tremor episodes. Their long duration (1–10^3 h) allowed us to define a statistical approach for characterizing the spectral content and polarization attributes (polarization degree, rectilinearity, horizontal azimuth and vertical incidence) of individual NB episodes. We found non-monochromatic NB episodes are not harmonics of a fundamental period. On the other hand, BB episodes were collectively analyzed since they showed a similar spectral and polarization-degree content.

A detailed comparison with activity reports and satellite images led us to classify the tremor episodes as eruptive and non-eruptive. By comparing characteristics of NB episodes with eruptive activity, no relationship was observed. However, the comparison of eruptive and non-eruptive episodes evinces an increase of linearly polarized waves for the former, and strong path or site effects controlling the wavefield of NB tremors.

BB tremors show a different pattern of occurrence since they can emerge individually or in multiple highly periodic episodes of swarms. More remarkably, swarm periods of BB episodes follow a seasonal behavior that coincides on numerous occasions with periods of ash emissions, and it would suggest a close relationship with the internal dynamics of the volcano.

Our observations raise significant questions about the origin of NB and BB tremors for further studies: What is the source mechanism behind the long duration of these tremors? How are gliding effects and seismic silences explained in non-eruptive episodes? And more essentially, what implications do BB tremors have for monitoring the Copahue volcano? Thus, forthcoming studies should be aimed to answer these questions, which can be addressed by deploying more stations (both conventional, seismoacoustic, or seismic arrays).

Finally, the approach followed here can be applied in limited monitoring conditions for characterizing and tracking volcanic tremor wavefield when C_P and C_L are ~ 1 and, therefore, enhance monitoring systems. In situations where more seismic stations are available, it can be applied for improving the knowledge of site or path effects in the tremor wavefield.

Appendix 1: Polarization analysis

The polarization content was analyzed by computing the attributes that describe the polarization ellipse, i.e., the rectilinearity, azimuth, and incidence. Since we work in the frequency domain, the degree of polarization needs to be computed firstly. This parameter quantifies to what extent the wavefield is polarized or, in other words, how well a polarization vector expresses the largest fraction of seismic energy in a unitary complex space (Samson 1983). The degree of polarization PD is mathematically expressed as (Samson and Olson 1980):

$$PD(f) = \frac{3\,\mathbf{tr}(\mathbf{W}^2(f)) - \mathbf{tr}^2(\mathbf{W}(f))}{2\,\mathbf{tr}^2(\mathbf{W}(f))}, \tag{3}$$

where $\mathbf{W}$ is the diagonal matrix resulting from the singular value decomposition (SVD) of the cross-spectral matrix (CSM), and **tr** denotes the trace function. The SVD also produces a 3×3 matrix that corresponds with the eigenvectors of the CSM (de Franco and Musacchio 2013). The polarization vector $\hat{\boldsymbol{d}}$ is defined as the eigenvector associated with the principal singular value at frequency f when the degree of polarization $P(f)$ is near the unity. Otherwise, when $P(f)$ is less than one, the direction of polarization is described by several polarized complex spaces and; hence, no clear direction contains the largest fraction of seismic energy (Park et al. 1987).

The polarization vector $\hat{\boldsymbol{d}}$ describes an elliptical particle motion at frequency f in a complex space. More generally, the three-component particle motion can be described by the real part of $A(t)e^{i\phi(t)}\hat{\boldsymbol{d}}$, where $A(t)$ is the phase-independent amplitude and $\phi(t)$ is the phase. Therefore, to evaluate the rectilinearity of the particle motion, we can rotate the polarization vector to orientate the two real vectors $\mathrm{Re}\{\hat{\boldsymbol{d}}\}$ and $\mathrm{Im}\{\hat{\boldsymbol{d}}\}$ in the direction of the semimajor and semiminor axis of the polarization ellipse (Morozov and Smithson 1996). Therefore, the rectilinearity R is defined by the ratio between the semiminor and semimajor axis, i.e.,

$$R = 1 - \frac{\left|\mathrm{Im}\{\hat{\boldsymbol{d}}\}\right|}{\left|\mathrm{Re}\{\hat{\boldsymbol{d}}\}\right|}, \quad \text{where } \left|\mathrm{Re}\{\hat{\boldsymbol{d}}\}\right| > \left|\mathrm{Im}\{\hat{\boldsymbol{d}}\}\right|. \tag{4}$$

We follow (Park et al. 1987) to derive the azimuth and incidence, which are schematically represented in Figure 14.

Azimuth Θ_H is measured counterclockwise from north by projecting $\hat{\boldsymbol{d}}$ in the horizontal plane, i.e.,

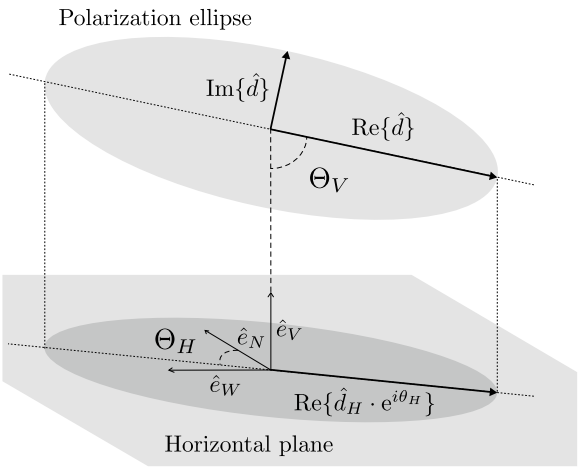

Fig. 14 Schematic illustration of polarization angles Θ_H and Θ_V based on (Park et al. 1987)

$\hat{\boldsymbol{d}}_H = \hat{\boldsymbol{d}} - (\hat{\boldsymbol{e}}_V \cdot \hat{\boldsymbol{d}})\hat{\boldsymbol{e}}_V$, being $\hat{\boldsymbol{e}}_V$ the vertical unitary direction. Then, rotating $\hat{\boldsymbol{d}}_H$ an angle θ_H in such that the horizontal displacement is maximum, Θ_H is finally expressed as:

$$\Theta_H = \arctan\left[\frac{\mathrm{Re}\{\hat{\boldsymbol{d}} \cdot \hat{\boldsymbol{e}}_W e^{i\theta_H}\}}{\mathrm{Re}\{\hat{\boldsymbol{d}} \cdot \hat{\boldsymbol{e}}_N e^{i\theta_H}\}}\right], \tag{5}$$

where $\hat{\boldsymbol{e}}_W$ and $\hat{\boldsymbol{e}}_N$ are the west and north unitary directions, respectively. Because the arc-tangent function is defined in the range $-90°$–$90°$, the azimuth angle Θ_H is defined in the range $0°$–$90°$ when $\mathrm{Re}\{\hat{\boldsymbol{d}}_V \cdot \hat{\boldsymbol{d}}^*_W\} < 0$ and $90°$–$180°$ when it is positive.

Incidence Θ_V is defined as the angle between the semimajor axis and the vertical, and it is computed similarly by searching an angle θ_V which maximizes the vertical displacement, i.e.,

$$\Theta_V = \arctan\left[\left|\frac{\mathrm{Re}\{\hat{\boldsymbol{d}} \cdot \hat{\boldsymbol{e}}_V e^{i\theta_V}\}}{\mathrm{Re}\{\hat{\boldsymbol{d}}_H e^{i\theta_V}\}}\right|\right], \tag{6}$$

on which the absolute value restricts Θ_V to be contained in the range $0°$–$90°$.

Abbreviations

BB: Broad-band; C_L: Linearly polarization coefficient of a characteristic peak; C_P: Polarization coefficient of a characteristic peak; PD: Polarization degree; pPSD: Most probable PSD; LOS: Line-of-sight; LST: Land surface temperatur; MVT: Maximum value of LST; NB: Narrow-band; N_H: Sample size of Θ_H of a characteristic peak; N_P: Sample size of PD of a characteristic peak; N_R: Sample size of R of a characteristic peak; N_T: Total sample size of a characteristic peak; N_V: Sample size of Θ_V of a characteristic peak; R: Rectilinearity; Θ_H: Horizontal azimuth; Θ_V: Vertical incidence.

Supplementary Information

The online version contains supplementary material available at https://doi.org/10.1186/s40623-021-01561-7.

Additional file 1: Tremor database. Data containing characterization of the 355 eruptive tremors separated according to its classification.

Additional file 2: The most probable PSD. Specific description of how the most probable PSD was computed.

Additional file 3: Activity Information. Information on the methods applied for tracking Copahue activity.

Additional file 4: Activity database. data containing activity information described in Additional file 3. An attribute of value 0 means "no" such as "No lake" or "No SO2", otherwise is 1.

Additional file 5: List of tables. List of tables supporting discussions.

Additional file 6: List of figures. List of figures supporting discussions.

Additional file 7: BB tremor and weather. Each image corresponds to a month and compares the weather conditions with BB tremors occurrence. Data in days provided by the AIC of Argentina. RH: Relative humidity. SWE: Snow water equivalent.

Acknowledgements

We express our gratitude to the Instituto Nacional de Prevención Sísmica (INPRES) of Argentina and the Autoridad Interjurisdiccional de Cuencas (AIC) of Argentina for sharing their data. We also thank the Canadian Space Agency for providing RADARSAT-2 data. We are grateful to Alicia Hotovec-Ellis, Arthur Jolly, and two anonymous reviewers for providing useful comments. In addition, special mention to Maurizio Rippepe, the Caviahue Municipality, Higinio del Monte, and Silvio Morales that collaborated in field works and helped with logistical support.

Authors' contributions

IM analyzed the data and drafted the manuscript. JA contributed to method construction and interpretation of the results. MH and AC described the geological settings and volcanic activity, and provided useful discussions. SS and DD analyzed SAR data and provided useful discussions. EM analyzed LST data and provided useful discussions. All authors read and approved the final manuscript.

Authors' information

IM is a PhD student with a CONICET scholarship (RD4868/15).

Funding

This research was partially supported by projects BRAVOSEIS (CTM2016.77315) of the Spanish Ministry of Science and PI40-A-548 of the National University of Rio Negro.

Availability of data and materials

The datasets used and/or analyzed during the current study are available from the corresponding author on reasonable request.

Declarations

Competing interests

The authors declare that they have no competing interests.

Author details

[1]Instituto de Investigación en Paleobiología y Geología, Universidad Nacional de Río Negro–CONICET, General Roca, Argentina. [2]Instituto Andaluz de Geofísica, Universidad de Granada, Granada, España. [3]Canada Centre for Mapping and Earth Observations, Natural Resources Canada, Ottawa, Canada. [4]European Centre of Geodynamics and Seismology, Walferdange, Luxembourg. [5]Centre Spatial de Liège, Université de Liège, Angleur, Belgium.

Received: 13 August 2021 Accepted: 13 December 2021
Published online: 04 January 2022

References

Agusto MR, Caselli A, Daga R, Varekamp J, Trinelli A, Dos Santos Afonso M, Velez ML, Euillades P, Ribeiro Guevara S (2017) The crater lake of Copahue volcano (Argentina): geochemical and thermal changes between 1995 and 2015. Geol Soc London Spec Publ 437(1):107–130. https://doi.org/10.1144/SP437.16

Almendros J, Ibáñez JM, Alguacil G, Del Pezzo E, Ortiz R (1997) Array tracking of the volcanic tremor source at Deception Island. Antarctica. Geophys Res Lett 24(23):3069–3072. https://doi.org/10.1029/97GL03096

Almendros J, Carmona E, Ibáñez J (2004) Precise determination of the relative wave propagation parameters of similar events using a small-aperture seismic array. J Geophys Res Solid Earth 109(B11):1–15. https://doi.org/10.1029/2003JB002930

Almendros J, Abella R, Mora M, Lesage P (2012) Time-dependent spatial amplitude patterns of harmonic tremor at arenal Volcano, Costa Rica: seismic-wave interferences? Bull Seismol Soc Am 102(6):2378–2391. https://doi.org/10.1785/0120120066

Almendros J, Abella R, Mora MM, Lesage P (2014) Array analysis of the seismic wavefield of long-period events and volcanic tremor at Arenal volcano, Costa Rica. J Geophysl Res Solid Earth 119(7):5536–5559. https://doi.org/10.1002/2013JB010628

Anderson S, Nehorai A (1996) Analysis of a polarized seismic wave model. IEEE Trans Signal Process 44(2):379–386. https://doi.org/10.1109/78.485933

Ayele A, Jacques E, Kassim M, Kidane T, Omar A, Tait S, Nercessian A, de Chabalier J-B, King G (2007) The volcano-seismic crisis in Afar, Ethiopia, starting September 2005. Earth Planet Sci Lett 255(1):177–187. https://doi.org/10.1016/j.epsl.2006.12.014

Bandt C, Pompe B (2002) Permutation entropy: a natural complexity measure for time series. Phys Rev Lett 88(17):174102. https://doi.org/10.1103/PhysRevLett.88.174102

Barcelona H, Yagupsky D, Vigide N, Senger M (2019) Structural model and slip-dilation tendency analysis at the Copahue geothermal system: inferences on the reservoir geometry. J Volcanol Geoth Res 375:18–31. https://doi.org/10.1016/j.jvolgeores.2019.03.007

Barrière J, D'Oreye N, Oth A, Theys N, Mashagiro N, Subira J, Kervyn F, Smets B (2019) Seismicity and outgassing dynamics of Nyiragongo volcano. Earth Planet Sci Lett 528:115821. https://doi.org/10.1016/j.epsl.2019.115821

Benoit JP, McNutt SR, Barboza V (2003) Duration-amplitude distribution of volcanic tremor. J Geophys Res Solid Earth 108(B3):1–15. https://doi.org/10.1029/2001JB001520

Candela-Becerra LJ, Toyos G, Suárez-Herrera CA, Castro-Godoy S, Agusto M (2020) Thermal evolution of the Crater Lake of Copahue Volcano with ASTER during the last quiescence period between 2000 and 2012 eruptions. J Volcanol Geoth Res 392:106752. https://doi.org/10.1016/j.jvolgeores.2019.106752

Cannata A, Di Grazia G, Montalto P, Ferrari F, Nunnari G, Patanè D, Privitera E (2010) New insights into banded tremor from the 2008–2009 Mount Etna eruption. J Geophys Res Solid Earth 115(12):1–22. https://doi.org/10.1029/2009JB007120

Carniel R (2014) Characterization of volcanic regimes and identification of significant transitions using geophysical data: a review. Bull Volcanol 76(8):1–22. https://doi.org/10.1007/s00445-014-0848-0

Caselli A, Agusto M, Velez ML, Forte P, Bengoa C, Daga R, Albite J, Capaccioni B (2016) The 2012 eruption. In Tassi F, Vaselli O, Caselli AT (eds.) Copahue Volcano, active volcanoes of the world chapter 4. Springer, Berlin Heidelberg, pp 61–77. https://doi.org/10.1007/978-3-662-48005-2.

Caudron C, Girona T, Jolly A, Christenson B, Savage MK, Carniel R, Lecocq T, Kennedy B, Lokmer I, Yates A, Hamling I, Park I, Kilgour G, Mazot A (2021) A quest for unrest in multiparameter observations at Whakaari/White Island volcano, New Zealand 2007–2018. Earth Planets Space 73(1):195. https://doi.org/10.1186/s40623-021-01506-0

Chouet B (1986) Dynamics of a fluid-driven crack in three dimensions by the finite difference method. J Geophys Res 91(B14):13967. https://doi.org/10.1029/jb091ib14p13967

Chouet B, Matoza R (2013) A multi-decadal view of seismic methods for detecting precursors of magma movement and eruption. J Volcanol Geoth Res 252:108–175. https://doi.org/10.1016/j.jvolgeores.2012.11.013

de Franco R, Musacchio G (2013) Polarization filter with singular value decomposition. Geophysics 78(3):932–938. https://doi.org/10.1190/1.1444983

Díaz J, Ruíz M, Crescentini L, Amoruso A, Gallart J (2014) Seismic monitoring of an alpine mountain river. J Geophys Res Solid Earth 119(4):3276–3289

Droznin DV, Shapiro NM, Droznina SY, Senyukov SL, Chebrov VN, Gordeev EI (2015) Detecting and locating volcanic tremors on the Klyuchevskoy group of volcanoes (Kamchatka) based on correlations of continuous seismic records. Geophys J Int. https://doi.org/10.1093/gji/ggv342

Ferrazzini V, Aki K, Chouet B (1991) Characteristics of seismic waves composing Hawaiian volcanic tremor and gas-piston events observed by a near-source array. J Geophys Res Solid Earth 96(B4):6199–6209. https://doi.org/10.1029/90JB02781

Ferrick MG, Qamar A, St. Lawrence W F (1982) Source mechanism of volcanic tremor. J Geophys Res 87(B10):8675–8683

Folguera A, Rojas Vera E, Vélez L, Tobal J, Orts D, Agusto M, Caselli A, Ramos VA (2016) A review of the geology, structural controls, and tectonic setting of Copahue Volcano, Southern Volcanic Zone, Andes, Argentina. In: Tassi F, Vaselli O, Caselli AT (eds) Copahue Volcano, Active Volcanoes of the World chapter 1. Springer-Verlag, Berlin Heidelberg, pp 3–22. https://doi.org/10.1007/978-3-662-48005-1.

Fujita E (2008) Banded tremor at Miyakejima volcano, Japan: implication for two-phase flow instability. J Geophys Res Solid Earth 113(4):1–18

Gestrich JE, Fee D, Tsai VC, Haney MM, Van Eaton AR (2020) A physical model for volcanic eruption tremor. J Geophys Res Solid Earth. https://doi.org/10.1029/2019JB018980

Girona T, Caudron C, Huber C (2019) Origin of shallow volcanic tremor: the dynamics of gas pockets trapped beneath thin permeable media. J Geophys Res Solid Earth 124(5):4831–4861

Goitom B, Oppenheimer C, Hammond JOS, Grandin R, Barnie T, Donovan A, Ogubazghi G, Yohannes E, Kibrom G, Kendall J-M, Carn SA, Fee D, Sealing C, Keir D, Ayele A, Blundy J, Hamlyn J, Wright T, Berhe S (2015) First recorded eruption of Nabro volcano, Eritrea, 2011. Bull Volcanol. https://doi.org/10.1007/s00445-015-0966-3

Goldstein P, Chouet B (1994) Array measurements and modeling of sources of shallow volcanic tremor at Kilauea Volcano, Hawaii. J Geophys Res Solid Earth 99(B2):2637–2652. https://doi.org/10.1029/93JB02639

Gottschämmer E (1999) Volcanic tremor associated with eruptive activity at Bromo volcano. Ann Geofis 42(3):465–481. https://doi.org/10.4401/ag-3731

Greenhalgh SA, Zhou B, Rutty M (2008) Effect of coherent noise on single-station direction of arrival estimation. J Seismolog 12(3):377–385. https://doi.org/10.1007/s10950-007-9085-8

Greenhalgh S, Sollberger D, Schmelzbach C, Rutty M (2018) Single-station polarization analysis applied to seismic wavefields: a tutorial. Adv Geophys 59:123–170. https://doi.org/10.1016/bs.agph.2018.09.002

Gresta S, Privitera E, Leotta A, Gasperini P (1996) Analysis of the intermittent volcanic tremor observed at Mt. Etna, Sicily during March-May 1987. Ann Geofis 39(2):421–428. https://doi.org/10.4401/ag-3979

Hantusch M, Lacanna G, Ripepe M, Montenegro V, Valderrama O, Farias C, Caselli A, Gabellini P, Cioni R (2021) Low-energy fragmentation dynamics at Copahue Volcano (Argentina) as revealed by an infrasonic array and ash characteristics. Front Earth Sci. https://doi.org/10.3389/feart.2021.578437

Hantusch M, Melchor I, Caselli A, Maria S, Da P (2021) Actividad sísmica precursora de las fases eruptivas de junio y julio de 2020 del volcán Copahue. Revista de la Asociacion Geologica Argentina 78(1):131–134

Hellweg M (2003) The polarization of volcanic seismic signals: medium or source? J Volcanol Geoth Res 128(1–3):159–176. https://doi.org/10.1016/S0377-0273(03)00252-X

Hotovec AJ, Prejean SG, Vidale J, Gomberg J (2013) Strongly gliding harmonic tremor during the 2009 eruption of Redoubt Volcano. J Volcanol Geoth Res 259:89–99. https://doi.org/10.1016/j.jvolgeores.2012.01.001

Hurst T, Hashimoto T, Terada A (2015) Crater Lake Energy and Mass Balance. In: Rouwet D, Christenson B, Tassi F, Vandemeulebrouck J (eds) Volcanic Lakes, Advances in Volcanology chapter 13. Springer-Verlag, Berlin Heidelberg, pp 307–321

Ibañez JM, Del Pezzo E, Bengoa C, Caselli A, Badi G, Almendros J (2008) Volcanic tremor and local earthquakes at Copahue volcanic complex, Southern Andes, Argentina. J Volcanol Geoth Res 174(4):284–294. https://doi.org/10.1016/j.jvolgeores.2008.02.005

Ichihara M, Matsumoto S (2017) Relative source locations of continuous tremor before and after the Subplinian events at Shinmoe-dake, in 2011. Geophys Res Lett 44(21):10871–10877. https://doi.org/10.1002/2017GL075293

Jiménez Morales V, Almendros J, Carmona E (2017) Detection of long-duration tremors at Deception Island volcano, Antarctica. J Volcanol Geoth Res 347:234–249. https://doi.org/10.1016/j.jvolgeores.2017.09.016
Jolly A, Caudron C, Girona T, Christenson B, Carniel R (2020) 'Silent' Dome emplacement into a wet Volcano: observations from an effusive eruption at White Island (Whakaari), New Zealand in late 2012. Geosciences 10(4):142. https://doi.org/10.3390/geosciences10040142
Julian BR (1994) Volcanic tremor: nonlinear excitation by fluid flow. J Geophys Res 99(B6):11859–11877
Konstantinou KI, Schlindwein V (2003) Nature, wavefield properties and source mechanism of volcanic tremor: a review. J Volcanol Geoth Res 119(1–4):161–187. https://doi.org/10.1016/S0377-0273(02)00311-6
Konstantinou KI, Ardiani MA, Sudibyo MR (2019) Scaling behavior and source mechanism of tremor recorded at Erebus volcano, Ross island, Antarctica. Phys Earth Planet Inter 290:99–106. https://doi.org/10.1016/j.pepi.2019.03.010
Lamberti MC, Vigide N, Venturi S, Agusto M, Yagupsky D, Winocur D, Barcelona H, Velez ML, Cardellini C, Tassi F (2019) Structural architecture releasing deep-sourced carbon dioxide diffuse degassing at the Caviahue - Copahue Volcanic complex. J Volcanol Geoth Res 374:131–141. https://doi.org/10.1016/j.jvolgeores.2019.02.004
Leet RC (1988) Saturated and subcooled hydrothermal boiling in groundwater flow channels as a source of harmonic tremor. J Geophys Res 93(B5):4835
Li KL, Gudmundsson O (2020) A probabilistic tremor location method. Geophys Res Lett 47(4):1–10. https://doi.org/10.1029/2019GL085538
Lundgren P, Nikkhoo M, Samsonov SV, Milillo P, Gil-Cruz F, Lazo J (2017) Source model for the Copahue volcano magma plumbing system constrained by InSAR surface deformation observations. J Geophys Res Solid Earth 122(7):5729–5747. https://doi.org/10.1002/2017JB014368
McMechan GA (1982) Resonant scattering by fluid-filled cavities. Bull Seismol Soc Am 72(4):1143–1153
McNutt SR, Nishimura T (2008) Volcanic tremor during eruptions: temporal characteristics, scaling and constraints on conduit size and processes. J Volcanol Geoth Res 178(1):10–18. https://doi.org/10.1016/j.urology.2015.07.047
Melchor I, Almendros J, Carniel R, Konstantinou KI, Hantusch M, Caselli A (2020) On data reduction methods for volcanic tremor characterization: the 2012 eruption of Copahue volcano, Southern Andes. Earth Planets Space 72(1):134. https://doi.org/10.1186/s40623-020-01270-7
Montegrossi G, Farina A, Fusi L, De Biase A (2019) Mathematical model for volcanic harmonic tremors. Sci Rep 9(1):14417. https://doi.org/10.1038/s41598-019-50675-2
Montenegro VM, Spagnotto S, Legrand D, Caselli AT (2021) Seismic evidence of the active regional tectonic faults and the Copahue volcano, at Caviahue Caldera. Bulletin of volcanology, Argentina. https://doi.org/10.1007/s00445-021-01442-7
Morales S, Franco L, Valderrama A, Cartes C (2015) Silencios sísmicos en la señal de tremor volcánico, como precursores inmediatos de explosiones durante octubre de 2014 en el volcán Copahue, Chile. (Spanish) [Seismic silences in volcanic tremor as an immediate explosion precursor during October 2014 in Copahue Volcano, Chile]. In: Actas del XIV Congreso Geológico Chileno, pp 69–71
Morozov IB, Smithson SB (1996) Instantaneous polarization attributes and directional filtering. Geophysics 61(3):872–881. https://doi.org/10.1190/1.1444012
Naismith AK, Matthew Watson I, Escobar-Wolf R, Chigna G, Thomas H, Coppola D, Chun C (2019) Eruption frequency patterns through time for the current (1999–2018) activity cycle at volcán de fuego derived from remote sensing data: evidence for an accelerating cycle of explosive paroxysms and potential implications of eruptive activity. J Volcanol Geoth Res 371:206–219. https://doi.org/10.1016/j.jvolgeores.2019.01.001
Nakano M, Kumagai H (2005) Response of a hydrothermal system to magmatic heat inferred from temporal variations in the complex frequencies of long-period events at Kusatsu-Shirane Volcano, Japan. J Volcanol Geoth Res 147(3–4):233–244. https://doi.org/10.1016/j.jvolgeores.2005.04.003
Neuberg J, O'Gorman C (2002) A model of the seismic wavefield in gas-charged magma: application to Soufrière Hills Volcano, Montserrat. Geol Soc London Memoirs 21(1):603–609. https://doi.org/10.1144/GSL.MEM.2002.021.01.29
Neuberg J, Pointer T (2000) Effects of volcano topography on seismic broadband waveforms. Geophys J Int 143(1):239–248. https://doi.org/10.1046/j.1365-246X.2000.00251.x
Neuberg J, Luckett R, Baptie B, Olsen K (2000) Models of tremor and low-frequency earthquake swarms on Montserrat. J Volcanol Geoth Res 101(1–2):83–104. https://doi.org/10.1016/S0377-0273(00)00169-4
Neuberg JW, Tuffen H, Collier L, Green D, Powell T, Dingwell D (2006) The trigger mechanism of low-frequency earthquakes on Montserrat. J Volcanol Geother Res 153(1–2 SPEC.ISS):37–50. https://doi.org/10.1016/j.jvolgeores.2005.08.008
Ogiso M, Matsubayashi H, Yamamoto T (2015) Descent of tremor source locations before the 2014 phreatic eruption of Ontake volcano, Japan 5. Volcanology. Earth Planet Space. https://doi.org/10.1186/s40623-015-0376-y
Park J, Vernon FL, Lindberg CR (1987) Frequency dependent polarization analysis of high-frequency seismograms. J Geophys Res 92(B12):12664
Park I, Jolly A, Kim KY, Kennedy B (2019) Temporal variations of repeating low frequency volcanic earthquakes at Ngauruhoe Volcano, New Zealand. J Volcanol Geoth Res 373:108–119. https://doi.org/10.1016/j.jvolgeores.2019.01.024
Park I, Jolly A, Matoza RS, Kennedy B, Kilgour G, Johnson R, Garaebiti E, Cevuard S (2021) Seismo-acoustic characterisation of the 2018 Ambae (Manaro Voui) eruption. Bull Volcanol. https://doi.org/10.1007/s00445-021-01474-z
Prieto G, Parker R, Vernon F III (2009) A Fortran 90 library for multitaper spectrum analysis. Comput Geosci 35:1701–1710. https://doi.org/10.1016/j.cageo.2008.06.007
Ripepe M, Gordeev E (1999) Gas bubble dynamics model for shallow volcanic tremor at Stromboli. J Geophys Res Solid Earth 104(B5):10639–10654
Roeoesli C, Walter F, Ampuero J-P, Kissling E (2016) Seismic moulin tremor. J Geophys Res Solid Earth 121(8):5838–5858. https://doi.org/10.1002/2015JB012786
Rust AC, Balmforth NJ, Mandre S (2008) The feasibility of generating low-frequency volcano seismicity by flow through a deformable channel. Geol Soc Spec Pub 307:45–56. https://doi.org/10.1144/SP307.4
Saccorotti G, Zuccarello L, Del Pezzo E, Ibanez J, Gresta S (2004) Quantitative analysis of the tremor wavefield at Etna Volcano, Italy. J Volcanol Geoth Res 136(3–4):223–245. https://doi.org/10.1016/j.jvolgeores.2004.04.003
Samson JC (1983) Pure states, polarized waves, and principal components in the spectra of multiple, geophysical time-series. Geophys J Int 72(3):647–664. https://doi.org/10.1111/j.1365-246X.1983.tb02825.x
Samson JC, Olson JV (1980) Some comments on the descriptions of the polarization states of waves. Geophys J Int 61(1):115–129. https://doi.org/10.1111/j.1365-246X.1980.tb04308.x
Seidl D, Schick R, Riuscetti M (1981) Volcanic tremors at Etna: a model for hydraulic origin. Bull Volcanol 44(1):43–56
Sherburn S, Scott BJ, Nishi Y, Sugihara M (1998) Seismicity at White Island volcano, New Zealand: a revised classification and inferences about source mechanism. J Volcanol Geoth Res 83(3–4):287–312. https://doi.org/10.1016/S0377-0273(98)00022-5
Takeo M (2021) Harmonic tremor model during the 2011 Shinmoe-dake eruption. Japan. Geophys J Int 224(3):2100–2120. https://doi.org/10.1093/gji/ggaa477
Tamburello G, Agusto M, Caselli A, Tassi F, Vaselli O, Calabrese S, Rouwet D, Capaccioni B, Di Napoli R, Cardellini C, Chiodini G, Bitetto M, Brusca L, Bellomo S, Aiuppa A (2015) Intense magmatic degassing through the lake of Copahue volcano, 2013–2014. J Geophys Res Solid Earth 120(9):6071–6084. https://doi.org/10.1002/2015jb012160
Tárraga M, Martí J, Abella R, Carniel R, López C (2014) Volcanic tremors: good indicators of change in plumbing systems during volcanic eruptions. J Volcanol Geoth Res 273:33–40. https://doi.org/10.1016/j.jvolgeores.2014.01.003
Unglert K, Jellinek AM (2015) Volcanic tremor and frequency gliding during dike intrusions at Kilauea-A tale of three eruptions. J Geophys Res Solid Earth 120(2):1142–1158. https://doi.org/10.1002/2014JB011596
Varekamp JC, Ouimette AP, Herman SW, Flynn KS, Bermudez A, Delpino D (2009) Naturally acid waters from Copahue volcano, Argentina. Appl Geochem 24(2):208–220. https://doi.org/10.1016/j.apgeochem.2008.11.018
Velez ML, Euillades P, Blanco M, Euillades L (2016) Ground deformation between 2002 and 2013 from InSAR observations. In: Tassi F, Vaselli O, Caselli AT (eds) Copahue Volcano, active volcanoes of the World chapter 8. Springer-Verlag, Berlin Heidelberg, pp 175–198. https://doi.org/10.1007/978-3-662-48005-2

Withers MM, Aster RC, Young CJ, Chael EP (1996) High-frequency analysis of seismic background noise as a function of wind speed and shallow depth. Bull Seismol Soc Am 86(5):1507–1515
Yukutake Y, Honda R, Harada M, Doke R, Saito T, Ueno T, Sakai S, Morita Y (2017) Analyzing the continuous volcanic tremors detected during the 2015 phreatic eruption of the Hakone volcano. Earth Planets Space 69(1):164. https://doi.org/10.1186/s40623-017-0751-y

Publisher's Note